EFFECT OF FIN SHAPES AND IMPINGING JETS ON HYDRO-THERMAL PERFORMANCE FOR SOLAR AIR HEATER

2023
MASTER THESIS
MECHANICAL ENGINEERING

Anas KABLAN

Thesis Advisor
Prof. Dr. Kamil ARSLAN

EFFECT OF FIN SHAPES AND IMPINGING JETS ON HYDRO-THERMAL PERFORMANCE FOR SOLAR AIR HEATER

Anas KABLAN

Thesis Advisor

Prof. Dr. Kamil ARSLAN

T.C.

Karabük University

Institute of Graduate Programs

Department of Mechanical Engineering

Prepared as

Master Thesis

KARABUK

August 2023

I certify that in my opinion the thesis submitted by Anas KABLAN titled "EFFECT OF FIN SHAPES AND IMPINGING JETS ON HYDRO-THERMAL PERFORMANCE FOR SOLAR AIR HEATER" is fully adequate in scope and quality as a thesis for the degree of Master of Science.

Prof. Dr. Kamil ARSLAN .....
Thesis Advisor, Department of Mechanical Engineering

This thesis is accepted by the examining committee with a unanimous vote in the Department of Mechanical Engineering as a Master of Science thesis. August 09, 2023

Examining Committee Members (Institutions)		Signature
Chairman :	Assist. Prof. Dr. Mehmet GÜRDAL (KU)	.....
Member :	Prof. Dr. Kamil ARSLAN (KBU)	.....
Member :	Assist. Prof. Dr. Mutlu TEKİR (KBU)	.....

The degree of Master of Science by the thesis submitted is approved by the Administrative Board of the Institute of Graduate Programs, Karabük University.

Prof. Dr. Müslüm KUZU .....
Director of the Institute of Graduate Program

"All the information in this thesis is attained and presented in agreement with ethical standards and disciplinary guidelines; I also affirm that I have given all due credit that doesn't appear in this work, as desired by these standards and guidelines."

Anas KABLAN

ABSTRACT

M. Sc. Thesis

EFFECT OF FIN SHAPES AND IMPINGING JETS ON HYDRO-THERMAL PERFORMANCE FOR SOLAR AIR HEATER

Anas KABLAN

Karabük University
Institute of Graduate Programs
The Department of Mechanical Engineering

Thesis Advisor:
Prof. Dr. Kamil ARSLAN
August 2023, 64 Pages

The simplest heating system for using solar thermal energy is a Solar Air Heater (*SAH*). The impacts of impinging jets and longitudinal fins on *SAH* have been investigated in this study. The absorber plate surface of *SAH* has been designed to have constant heat flux condition. Numerical studies have been performed under turbulent flow condition (10,000≤ *Re*≤25,000). Shear Stress Transport (*SST*) *k-ω* turbulence model has been used. By using *ANSYS* Fluent 2020 R2, simulations of *3-D* Computational Fluid Dynamics (*CFD*) have been done. An in-depth analysis has been done for determination of the impacts of fin height, fin shape, and mass flow rate on thermal efficiency ($\acute{\eta}$) of *SAH*.

It was obtained from the numerical results that using impingement jets and adding longitudinal fins improve the Nusselt number (*Nu*) and thermal efficiency. The findings indicated that optimal thermal efficiency and Nusselt numbers are achieved

with smaller fin heights when a lower Reynolds number is applied. As the increasing Reynolds number, higher fin heights have led to improve thermal efficiencies. It was also determined that altering the fin height has minimal impact on pressure drop. Circular and triangular fins exhibited lower pressure drop values compared to rectangular fins. It has been determined that using impinging jets increases the thermal efficiency of the *SAH*. The highest thermal efficiency (74.354%) and Nusselt number (222.645) have been achieved at *Re*=25000 for the rectangular fin design with height of 3.75 *mm*.

Key Words **:** Impinging Jet, *CFD*, Fin, Solar Air Heater, Forced Convection, Solar Energy.

Science Code : 91412

ÖZET

Yüksek Lisans Tezi

HAVALI GÜNEŞ KOLLEKTÖRLERİNDE KANATÇIK ŞEKİLLERİ VE ÇARPAN JETLERİN HİDROTERMAL PERFORMANSA ETKİSİ

Anas KABLAN

Karabük Üniversitesi
Lisansüstü Eğitim Enstitüsü
Makina Mühendisliği Anabilim Dalı

Tez Danışmanı:
Prof. Dr. Kamil ARSLAN
Ağustos 2023, 64 sayfa

Güneşin ısıl enerjisini kullanmak için en basit ısıtma sistemi Havalı Güneş Kollektörü'dür (*HGK*). Bu çalışmada çarpan jetlerin ve kollektör boyunca yerleştirilmiş kanatçıkların *HGK* üzerindeki etkileri araştırılmıştır. *HGK*'nın yutucu plaka yüzeyi sabit ısı akısı koşuluna sahip olacak şekilde tasarlanmıştır. Sayısal çalışmalar türbülanslı akış koşulunda ($10.000 \leq Re \leq 25.000$) yapılmıştır. Shear Stress Transport (*SST*) k-ω türbülans modeli kullanılmıştır. *ANSYS* Fluent 2020 R2 kullanılarak 3 Boyutlu Hesaplamalı Akışkanlar Dinamiği (*HAD*) simülasyonları gerçekleştirilmiştir. Kanatçık yüksekliği, kanat şekli ve kütle akış hızının *HGK* ısıl verimliliği (η) üzerindeki etkilerinin belirlenmesi için derinlemesine bir analiz yapılmıştır.

Sayısal çalışma sonuçlardan çarpan jetlerinin kullanılması ve boyuna kanatçık eklenmesinin Nusselt sayısını (*Nu*) ve ısıl verimi iyileştirdiği elde edilmiştir. Bulgular,

daha düşük Reynolds sayısı uygulandığında daha küçük kanatçık yükseklikleriyle optimum ısıl verim ve Nusselt sayılarının elde edildiğini göstermiştir. Reynolds sayısının artmasıyla birlikte daha yüksek kanatçık yükseklikleri ısıl verimin artmasına neden olmuştur. Ayrıca, kanatçık yüksekliğinin basınç düşüşü üzerinde minimum etkiye sahip olduğu belirlenmiştir. Dairesel ve üçgen kanatçıklar, dikdörtgen kanatçıklara göre daha düşük basınç düşümü değerleri sergilemişlerdir. Çarpan jetlerin kullanılmasının *HGK*'nın ısıl verimini arttırdığı belirlenmiştir. En yüksek ısıl verim (%74,354) ve Nusselt sayısı (222,645) 3,75 *mm* yüksekliğindeki dikdörtgen kanatçık tasarımında *Re*=25000 için elde edilmiştir.

Anahtar Kelimeler : Çarpan Jet, *HAD*, Kanatçık, Havalı Güneş Kollektörü, Zorlanmış Taşınım, Güneş Enerjisi.

Bilim Kodu **:** 91412

ACKNOWLEDGEMENT

I will be eternally grateful to my family, particularly my parents, wife, and all of my brothers and sisters, for their unending support, patience, and generosity. In addition, I would like to thank my supervisor, Prof. Dr Kamil ARSLAN, for providing insights and guidance, in addition to patience with my job conditions throughout my thesis research. I've had excellent academic performance under his supervision. Finally, I don't forget to thank my colleague M.Sc. Hayati Kadir PAZARLIOĞLU for advising me throughout my project work.

CONTENTS

Page

APPROVAL ii
ABSTRACT iv
ÖZET vi
ACKNOWLEDGEMENT viii
CONTENTS ix
LIST OF FIGURES xii
LIST OF TABLES xv
SYMBOLS AND ABBREVIATIONS INDEX xvi

PART 1 1
INTRODUCTION 1
1.1. HEAT TRANSFER 2
1.2. FUNDAMENTALS OF IMPROVED SOLAR AIR HEATER (*SAH*) 3
1.2.1. *SAH* Components 4
1.2.2. Working Principle Of *SAH* 6
1.3. LITERATURE REVIEW 6
1.4. OBJECTIVE AND AIM OF THE STUDY 11

PART 2 13
METHODOLOGY 13
2.1. PROBLEM DESCRIPTION 13
2.1.1. *SAH* With Impinging Jets 14
2.1.2. Finned *SAH* With Impinging Jets 17
2.2. ASSUMPTIONS AND CONSTANTS 19
2.2.1. Assumptions 19
2.2.2. Constants 19
2.3. THERMOPHYSICAL PROPERTIES 20

Page

2.4. GOVERNING EQUATIONS AND BOUNDARY CONDITIONS 20
2.4.1. Governing Equations 20
2.4.2. *SST k-ω* Turbulence Model Equations 21
2.4.3. Boundary Conditions 22
2.4.4. Reynolds Number 23
2.4.5. Turbulence Intensity 24
2.4.6. Nusselt Number 24
2.4.7. Pressure Drop 25
2.4.8. Total Plate Loss Coefficient 25
2.4.9. Useful Energy Gain 26
2.4.10. Thermal Efficiency Of The System 27
2.5. NUMERICAL MODEL 27
2.5.1.Geometry Modeling 27
2.5.2. Mesh 27
2.5.3. Models 30
2.5.4. Methods 30
2.5.5. Solution Controls 31
2.5.6. Simulation Residuals 31
2.5.7. Initialization 32
2.6. NUMERICAL STUDY VALIDATION 32

PART 3 34
RESULTS AND DISCUSSIONS 33
3.1. *SAH* SIMULATION 34
3.1.1. Velocity Vectors 34
3.1.2. Temperature Distribution 36
3.1.2.1. Smooth Absorber Plate Surface Temperature Distribution 36
3.1.2.2. Finned Absorber Plate Surface Temperature Distribution 37
3.1.3. Nusselt Number Distribution 39
3.1.3.1. Smooth Collector Surface Nusselt Number Distribution 39
3.1.3.2. Finned Collector Surface Nusselt Number Disribution 40

Page

3.1.4. Pressure Distribution 42
3.1.4.1. Smooth Colector Surface Pressure Distribution 42
3.1.4.2. Finned Colector Surface Temperature Distribution 43
3.2. PARAMETRIC STUDIES 45
3.2.1. Comparing the Fin Shapes 46
3.2.1.1. Rectangular Fin Shape 46
3.2.1.2. Circular Fin Shape 49
3.2.1.3. Triangular Fin Shape 52
3.2.2. Comparison Of The Effects Of All Variable On The System Performance 55

PART 4 59
CONCLUSION 59
SUGGESTION FOR FUTURE WORK 60

REFERENCES 61

RESUME 64

LIST OF FIGURES

Page

Figure 1.1. Natural (free) convection heat transfer mechanism 2
Figure 1.2. Forced convection heat transfer mechanism 3
Figure 1.3. *SAH* Components 5
Figure 1.4. *SAH* working principles 6
Figure 2.1. Numerical analysis methodology chart 13
Figure 2.2. *SAH* length and width dimensions 15
Figure 2.3. *SAH* height dimansion 15
Figure 2.4 Jet locations and dimesions 16
Figure 2.5. Dimensions of the rectangular fins 17
Figure 2.6. Dimensions of the circular fins 17
Figure 2.7. Dimensions of the triangular fins 18
Figure 2.8. *3D* model view of the *SAH* with impinging jets and longitudinal fins. 18
Figure 2.9. Smooth *SAH* mesh 28
Figure 2.10. Finned *SAH* mesh 29
Figure 2.11. Inflation layers 29
Figure 2.12. Solution methods properties 30
Figure 2.13. Residuals values Click or tap here to enter text. 31
Figure 2.14. Residuals with iterations 32
Figure 2.15. Numerical simulation results and experimental data 33
Figure 3.1. *3D* view of the velocity vector distribution 35
Figure 3.2. Side view (*XY* plane) of the velocity vector distribution 35

Page

Figure 3.3. Velocity vector distribution through the impinging jets. 35
Figure 3.4. Temprature distribution on the absorber plate for Re=10000 36
Figure 3.5. Temprature distribution on the absorber plate for Re=15000 36
Figure 3.6. Temprature distribution on the absorber plate for Re=20000 37
Figure 3.7. Temprature distribution on the absorber plate for Re=25000 37
Figure 3.8. Temprature distribution on the absorber plate with fins for Re=10000 .. 38
Figure 3.9. Temprature distribution on the absorber plate with fins for Re=15000 .. 38
Figure 3.10. Temprature distribution on the absorber plate with fins for Re=20000 38
Figure 3.11. Temprature distribution on the absorber plate with fins for Re=25000 39
Figure 3.12. Nusselt Number distribution on the absorber plate for Re=10000 39
Figure 2.13. Nusselt Number distribution on the absorber plate for Re=15000 40
Figure 3.14. Nusselt Number distribution on the absorber plate for Re=20000 40
Figure 3.15. Nusselt Number distribution on the absorber plate for Re=25000 40
Figure 3.16. Nusselt Number distribution on the absorber plate with fins for Re=10000 41
Figure 3.17. Nusselt Number distribution on the absorber plate with fins for Re=15000 41
Figure 3.18. Nusselt Number distribution on the absorber plate with fins for Re=20000 41
Figure 3.19. Nusselt Number distribution on the absorber plate with fins for Re=25000 42
Figure 3.20. *3-D* view of pressure distribution on the smooth absorber 42
Figure 2.21. *3-D* zoomed-in view of pressure distribution on the smooth absorber .. 43
Figure 3.22. Top view of pressure distribution on the smooth absorber 43
Figure 3.23. *3-D* view of pressure distribution on the finned absorber 44
Figure 3.24. *3-D* zoomed-in view of pressure distribution on the finned absorber ... 44
Figure 3.25. Top view of pressure distribution on the finned absorber 45
Figure 3.26. Variation of efficiency with Reynolds number for all fin's height values 47
Figure 3.27. Variation of *Nu* with Reynolds number for all fin's height values 48
Figure 3.28. Variation of ΔP with Reynolds number for all fin's height values 49

Page

Figure 3.29. Variation of efficiency with Reynolds number for all fin's height values 50
Figure 3.30. Variation of *Nu* with Reynolds number for all fin's height values..... 51
Figure 3.31. Variation of *ΔP* with Reynolds number for all fin's height values 52
Figure 3.32. Variation of efficiency with Reynolds number for all fin's height values 53
Figure 3.33. Variation of *Nu* with Reynolds number for all fin's height values..... 54
Figure 3.34. Variation of *ΔP* with Reynolds number for all fin's height values 55
Figure 3.35. Variation of ή with fin height for all fin shapes at all values of *Re*..... 56
Figure 3.36. Variation of *Nu* with fin height for all fin shapes at all values of *Re* 57
Figure 3.37. Variation of *ΔP* with fin height for all fin shapes at all values of *Re* 58

LIST OF TABLES

Page

Table 2.1. Dimensions of *SAH* with impinging jets 16

Table 2.2. Dimensions of fins 18

Table 2.3. The constants used in the study 19

Table 2.4. Thermophysical properties of the Air and Aluminum used in this study 20

Table 2.5. System boundary conditions 22

Table 2.6. Solution Controls for under relaxation factors 31

Table 2.7. Percent error between the numerical simulations results and experimental data 33

Table 3.1. Results of the smooth *SAH* with impinging jets 45

Table 3.2. Results of the *SAH* with impinging jets and rectangular fins. 46

Table 3.3. Results of the *SAH* with impinging jets and circular fins. 49

Table 3.4. Results of the *SAH* with impinging jets and triangular fins. 52

SYMBOLS AND ABBREVIATIONS INDEX

SYMBOLS

A	: inlet area, m^2
A_p	: area of the absorber plate, m^2
C	: empirical factor
C_p	: specific heat, $J/kg.K$
D_h	: hydraulic diameter, m
D_{jet}	: jet diameter, m
D_ω	: Cross-diffusion term
e	: empirical factor
f	: empirical factor
$\tilde{G}_k$	: generation of the turbulent kinetic energy (k) due to mean velocity gradients
G_ω	: generation of the specific dissipation rate (ω)
H	: thickness of the bottom plate, m
h	: average convection heat transfer coefficient, $W/m^2.K$
h_{jet}	: convection heat transfer coefficient of the jets, $W/m^2.K$
h_w	: wind heat transfer coefficient, $W/m^2.K$
I	: solar radiation intensity, W/m^2
$I_{\substack{turbulent \\ intensity}}$	: turbulent intensity

k : thermal conductivity, $W/m.K$

N : number of glass cover

Nu : Nusselt number

P : inlet parameter, m

Q_u : useful energy gain, W

q'' : heat flux, W/m^2

Re : Reynolds number

S : absorber solar radiation, W/m^2

$S_k \; and \; S_\omega$: User-define source terms

T_a : ambient temperature, K

T_b : average inlet and outlet temperature, K

T_{in} : inlet temperature, K

T_{pm} : main plate temperature, K

T_{out} : outlet temperature, K

U_b : bottom plate loss coefficient, $W/m^2.K$

U_L : total plate loss coeffecient, $W/m^2.K$

U_t : top plate loss coeffecient, $W/m^2.K$

V_w : wind velocity, m/s

v_{in} : inlet velocity, m/s

Y_k : dissipation rate of kinetic energy (k) caused by the turbulence

Y_ω : dissipation rate of ω caused by the turbulence

y^+ : normalized distance from the wall

β : collector Degree, ^{o}

ΔP : pressure drop, kPa

ε_g : emissivity of the cover

ε_p : emissivity of the plate

ɳ : thermal efficiency

v : kinematic viscosity, m^2/s

ρ : density, kg/m^3

σ : Stefan-Boltzman Constant, W/m^2K^4

$\tau\alpha$: transmittance–absorptance

ω : Specific dissipation rate

ABBREVIATIONS

CFD : Computational Fluid Dynamics

SAH : Solar Air Heater

SST : Shear Stress Transport

PART 1

INTRODUCTION

The global need for energy is growing faster than predicted, in tandem with population growth, the cost of this type of power is dropping every day. As traditional energy sources severely damage human health, produce environmental degradation, and contribute to global warming. The demand for nonrenewable energy sources is steadily declining. Therefore, there is need to take advantage of a type of energy sufficient for people and safe for both nature and people. Solar energy and other renewable energy forms are the first to come to mind [1].

Flat plate Solar Air Heater (*SAH*) is frequently categorized as an energy application device with a low temperature grade that requires temperatures value between 60 °*C* and 100 °*C*. It is mostly used for internal space heating, drying of woods and agricultural goods, etc. *SAH* is typically employed as heat exchangers to convert the solar irradiation that has been received into heat energy. However, the *SAH's* thermal performance is subpar because of the weak thermal conductivity, low heat capacity, and low density of air. Recent studies found that the impinging jet approach in *SAH* was used as an efficient way to boost its efficiency [2].

Fins are also the most common heat transfer augmentation features used to promote the heat transfer from the heated wall in *SAH* to the working fluid. Fins, however, cause an increment in pressure loss of the flow. Results show that heat transfer and conversion potential increase with fin efficiency [3].

1.1. HEAT TRANSFER

Heat transfer occurs through conduction, convection, or radiation. A medium with a greater temperature transfers heat to one with a lower temperature [4]. Conduction is the thermal energy transfer of a substance, which may be a gas, liquid, or solid, from neighboring highly energetic particles to low energetic ones. In liquid and gaseous substances random molecule movement emerges as molecules collide and dispersion. In solids, it results from the interaction of the lattice-based molecules trembling and unbound electrons transferring energy [5]. Convection heat transfer is the one of the types of heat transfer that uses the integrated influences of conduction and movements of fluid to transfer energy from a solid surface to the nearby moving liquid or gas and vice versa. Convection heat transfer is increased by high velocity moving fluid. Heat transfer between a solid surface and the surrounding fluid occurs only by conduction in the absence of any bulk fluid motion [6,7]. Although the bulk motion of the fluid promotes heat transfer between the solid surface and the fluid. It also makes calculating heat transfer rates more challenging. Natural and forced convection heat transfers are the two different types of convection heat transfer [8].

Free convection heat transfer occurs when the fluid moves with the buoyancy forces caused by the variation of density of the fluid brought about by changes in the fluid's temperature [9]. Figure 1.1 presents the free convection heat transfer mechanism.

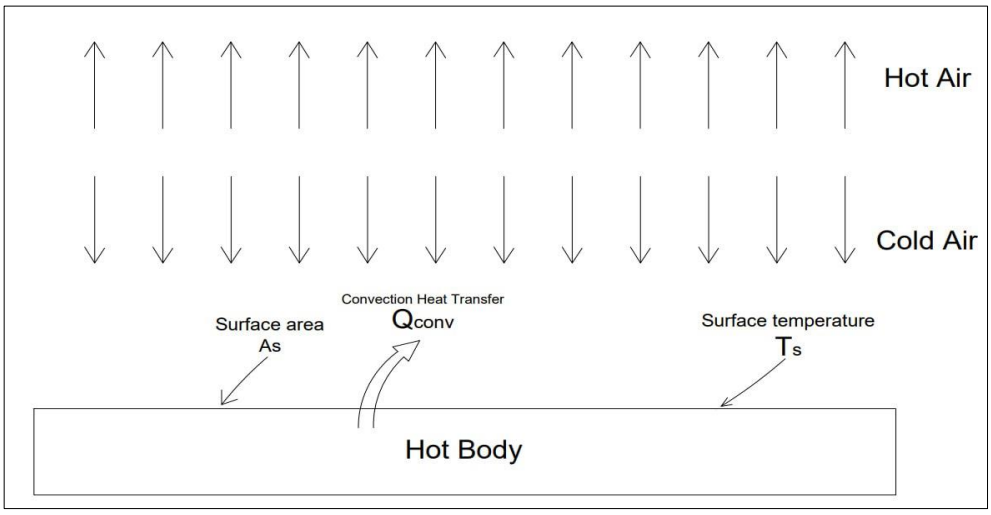

Figure 1.1. Natural (free) convection heat transfer mechanism.

Forced convection is a form of thermal energy transfer that occurs by forcing fluid to get it moving to facilitate heat transfer [10]. This may be accomplished with a fan, a compressor, a blower, or another device. Figure 1.2 explains how the forced convection heat transfer works. The forced type of convection heat transfer achieved in this study by applying the impinging jets on the surface of the *SAH* to enhance the removal of heat and give it more chance to take more solar energy [11].

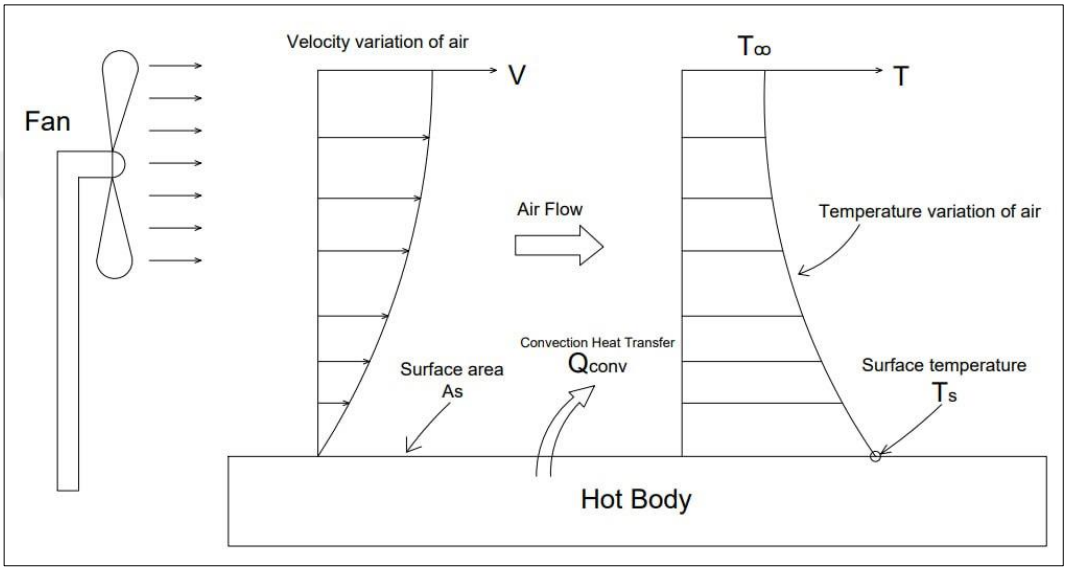

Figure 1.2. Forced convection heat transfer mechanism.

Radiation, a captivating phenomenon, emerges when matter emits electromagnetic waves, or photons, due to intricate alterations in the electronic configurations of atoms or molecules. Unlike conduction and convection, the conveyance of heat through radiation necessitates no intermediary medium, granting it an extraordinary quality. Remarkably, even in the vacuum of space, heat transfer by radiation remains unaffected, moving at the astonishing speed of light [12].

1.2. FUNDAMENTALS OF IMPROVED SOLAR AIR HEATER (*SAH*)

Why to use impinging jets and different shapes of longitudinal fins? The target results of this study are indicating that how the combination of placing longitudinal fins on the absorber surface and using impinging jet affects the thermal efficiency of *SAH*.

It is an application that relies on solar radiations to produce energy using forced convection to produce power by continuous cooling of the absorber plate with air pumped by the impinging jets. The impinging jet technology is widespread used in many applications such as the cooling of electronic components and turbine blades [13]. Various investigations on the jet impingement approach for improving heat transfer rate have been conducted in the past. This method was primarily employed for gas turbine cooling [14]. It is possible to enhance *SAH* efficiency using impinging air jets rather than parallel flow to increase the heat transfer from the heated absorber plate to the air passing through the duct.

This procedure typically entails placing a jet plate beneath the absorber plate and outfitting it with an arrangement of circular punctures, allowing air to be compressed vertically on the absorber plate. Because of the narrower flow path and higher turbulence, these air jets may eliminate a lot of heat. This is due to higher heat transfer coefficient values in the regional zones, which leads to improve the thermal efficiency. This method's primary drawback is the rise in fricative wastage and pneumatic power costs brought on by the greater air duct pressure drop, which reduces the thermo-hydraulic of these types of *SAH* [15]. Because of the basic work principle, the *SAH* can operate essentially in any kind of environment and, Needless to say, it works better outside on sunny days. To reduce the expenses of conducting an excessive number of real experiments, a numerical technique known as Computational Fluid Dynamics (*CFD*), simplifies and eases the way of this research.

1.2.1. *SAH* Components

SAH is built of:

- Insulation at the bottom to avoid wasting energy.
- Air inlet.
- Jet plate to force the air entered to the system. It is a high effective way to accelerate heat transfer over a surface is by jet impingement cooling. It has many uses in engineering, including cooling electrical components and turbine blades [16]. Impinging jets can produce turbulent flow regimes and induce vortices, which can

accelerate mixing and raise the coefficient of heat transfer to increase the heat energy transmitting rates.

- Air outlet.
- Fins are extended surfaces attached to a primary surface to increase the exposed area available to improve convection heat transfer [17]. Both the *SAH* efficiency and convective heat transfer can be considerably improved. Additionally, fins can heighten the gradient of the surface temperature, which can quicken the pace of heat transfer to boost the absorbed power by raising the region of transferring heat by increase cooling of the absorber from the bottom surface of the exposed wall heated to make more chances of absorbing energy from the top.
- Absorber plate (wall heated) that takes the solar radiations to convert them into usable energy. Copper, stainless steel, or plastic are used to make the absorber plate. The entire absorbent's superficies is encased in absorbent black materials. The absorptivity can be increased by applying a selective coating to the copper absorber plate, and a glass cover [18]. All of the *SAH* components and the air motion are expressed as side and front views in Figure 1.3.

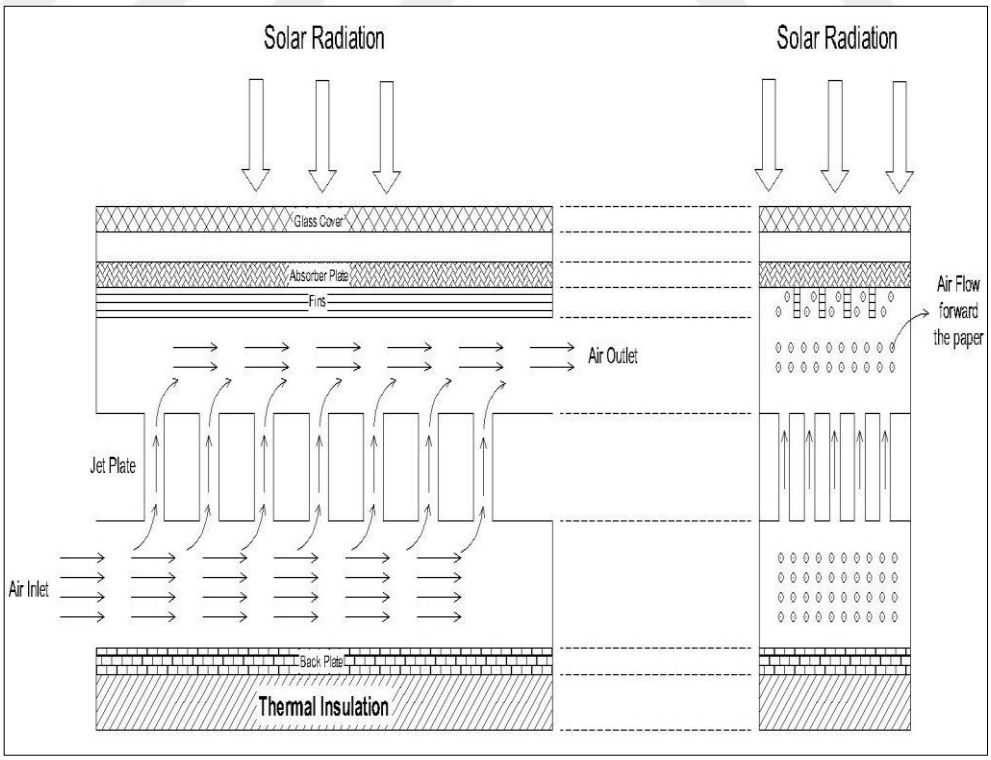

Figure 1.3. *SAH* components.

1.2.2. Working Principle of *SAH*

Forced convection is one of the most prevalent typical forms of convective heat transfer. This research uses an absorber plate that captures solar radiation and transforms it into usable energy. After air enters the *SAH*, it is forced toward the absorber plate's finned bottom surface to cool the surface by exposing the fins to impinging air to increase the heat transfer area. Figure 1.4 explains how system is working and how the air is moving through the *SAH*.

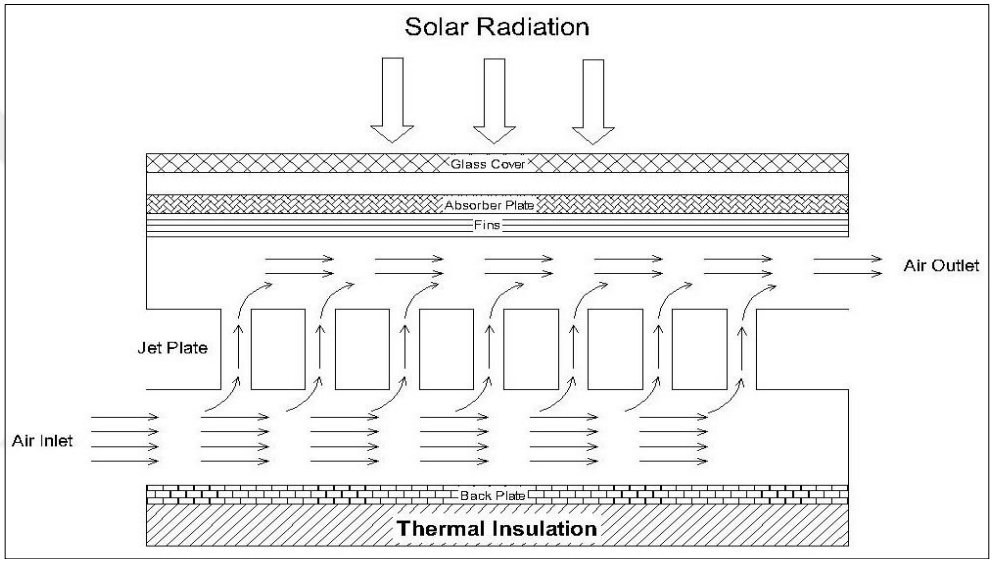

Figure 1.4. *SAH* working principles.

1.3. LITERATURE REVIEW

This section serves as a comprehensive exploration of existing research and scholarly works related to a *SAH*. It plays a crucial role in providing a foundation for understanding the current state of knowledge, identifying gaps, and highlighting the significance of the research under consideration. This section aims to delve into the wealth of insights offered by prior studies, offering context and a launching point for the research at hand. As we embark on this literature review journey, we will navigate through a diverse array of studies, analyses, and perspectives that have contributed to the understanding of our chosen subject. By critically examining the existing body of work, we can unveil trends, contradictions, and areas that warrant further investigation.

This synthesis of knowledge will not only inform our research but also aid in shaping a solid framework that propels us towards meaningful contributions to the field.

Moummi et al. [19] explored the effect of adding rectangular fins orthogonal to the airflow. The fluid is distributed evenly and the amount of inert areas is decreased by flowing out through the voids separating fins in a single row. They found that when the volumetric flow rate rises, efficiency rises as well. One also observes that an asymptotic regime was attained and that this regime is the one in which the increase in volumetric flow rate is meaningless. With the insertion of fins, efficiency rises. Efficiency was improved by 30% higher in the *SAH* with fins than in the smooth one.

Kumar et al. [20] studied adding fins to solar air heaters and found that herringbone corrugated fins connected along the fluid flow channel below the absorbing surface improved the efficacy of the *SAH* collector. Through operational aspects like mass flow rate, system characteristics like fin pitch, fin spacing ratio, and flow cross section aspect ratio, as well as metrological elements like sun intensity, the thermal performance of the herringbone corrugated finned *SAH* is investigated. It is demonstrated that the thermal efficiency of the conventional solar air heater increases from 36.2% to 56.6% with a fin pitch of 2.5 *cm* and a fixed mass flow rate of 0.026 *kg/s*, albeit at a high cost of the pressure drop.

KARIM et al. [21] studied theoretically and experimentally about heat transfer characteristics of flat plate, finned, and v-wavy solar air heaters, to enhance the performance of conventional *SAH*. The results demonstrated that the v-waved collector exhibited a remarkable 10-15% higher efficiency compared to flat plate collectors and a 5-9% higher efficiency than finned collectors. The increased heat transfer area played a pivotal role in boosting the efficiency of both finned and v-waved collectors. Notably, the v-waved collector possessed a significant advantage in absorbing a greater quantity of solar radiation compared to a flat plate and finned collectors with equal absorptivity. This superiority stemmed from the phenomenon of multiple reflections and absorption of incident radiation. Consequently, the v-wavy solar air heater shows immense promise for advancing the efficiency and effectiveness of solar energy utilization.

Aboghrara et al. [22] investigated with an experimental study of impinging jets assembled with a wavy absorber wall and making a disparity with the classical type of it, to know how the waves in an absorbing plate affect the execution of the system. The impact of air mass inflow rate and solar radiances on effectiveness and outflow air temperature is examined. Results indicate that a crucial factor in perfecting heat transfer is the inflow spurt smash on the wavy wall absorber. According to the results of the current trial, solar air heaters' capability to transfer heat is significantly told by the mass inflow rate of air. It has been set up that the proposed design's conduit's thermal effectiveness is nearly 14 % more advanced than the traditional smooth channel.

Safitra et al. [23] carried out an experimental investigation under practical circumstances starting from 9:00 *am* to 6:00 *pm*. to determine the thermal performance of *SAH* with rectangular fins *SAH* at low air velocity. The outcome demonstrates that at 12:00 *pm*, smooth *SAH* without fins had the lowest air outlet temperature of 52°*C* and the highest thermal efficiency of 48.47%. While *SAH* with rectangular fins had the maximum air outlet temperature of 62°*C* and the highest thermal efficiency of 76,68%, it was positioned staggered with a 30° tilt angle. At noon and a tilt of 0°, the thermal efficiency of *SAH* with rectangular fins is 29.67% greater than without fins. *SAH* has a 25.26 % thermal efficiency with rectangular fins. At a 30° inclination at noon, the thermal efficiency of *SAH* with rectangular fins is 25.26% higher than smooth ones. The functioning of a solar air heater can be improved by high heat transfer. In order to improve effectiveness, a tilt's slope affects how solar heat is distributed.

Nayak et al. [24] carried out an experimental investigation was on solar air heaters, designed in various configurations, considering both laminar and turbulent flow regimes. The study focused on an operating range of $2700 \leq Re \leq 6900$. The solar air heaters were tested with a 22.6° attack angle, and the effects of the distance of the jet to the absorber surface and the arrangement of the jet array were examined in mixed order. The experiments were conducted in the Indian region between November and December, with recordings taken from 9:00 *am* to 3:00 *pm*. The evaluation of the findings was based on the outlet temperature, collector efficiency, and Nusselt number (*Nu*). The results revealed that the Nusselt number and exit temperature were at their

lowest when the distance of the jet to the absorber surface was the greatest. Conversely, the mixed jet array exhibited the highest Nusselt number and exit temperature compared to the ordered jet array. Furthermore, the best collector efficiency was achieved when the jet was placed closest to the absorber surface, and the jet arrangement was in a mixed configuration.

Bhushan et al. [25] conducted an experimental investigation using both a smooth plate and a dimpled plate *SAH* on bright, sunny days. Under turbulence flow conditions ($5500 \leq Re \leq 10300$), the trials were conducted from 9:30 *am* to 2:30 *pm* on 6 days, with 6 varied flow rates varying from 28×10^{-3} *kg/s* to 51×10^{-3} *kg/s*. A numerical analysis of the results revealed that the dimpled form of *SAH* produced more useful energy than the smooth one. In addition, it was found that the dimpled heater's effective efficiency did not significantly rise at greater mass flow rates, making it less appropriate for high-flow rate applications. The smooth *SAH's* efficient power output ranged from 1.5 *W* to 165 *W*, whereas the dimpled *SAH's* ranged from 8 *W* to 207 *W*. Around 12:30 *pm*, the performance was at its peak, while the morning hours had the lowest performance. The study contrasted the energy losses of the two varieties of heaters. It was determined that the dimpled *SAH* had decreased energy loss because the structure of the dimples maximized the amount of useful heat gain.

Yadav et al. [26] performed a numerical analysis of the mechanism of heat transfer in a *SAH* employing an absorber plate that has an impinging jet. The *RNG* k-turbulence model was used in *CFD* modelling. The jet diameter ratio and jet height ratio, with variations of 0.065 to 0.195 and 0 to 0.433, respectively, were the system characteristics taken into account. In the variation of ($3500 \leq Re \leq 17{,}500$), the effectiveness of *SAH* with the impinging jet was evaluated under various flow situations. On the absorber plate, a constant heat flux of 1000 W/m^2 was applied. The investigation found that for all *Re* values, the flat plate *SAH* had the lowest Nusselt number. As a result, it was discovered that the *SAH* with an impingement jet had a better capacity for heat transfer than *SAH* with a flat plate. At a jet diameter ratio of 0.065 and a jet height ratio of 0.216 when *Re*= 17500, the greatest heat transfer was realized. The Nusselt number decreased past a jet diameter ratio of 0.065 as a result of

interaction between nearby jets. The distribution of the jet decreased near the heated surface as the jet diameter increased due to increased jet interaction.

Singh et al. [27] have done a study about the heating capacity of the different number of wavy finned *SAH* in comparison to a smooth surface *SAH*, the variation in numbers of fins is 15, 20, and 25. The maximum absorber plat temperature results are 380.6 *K*, 374.6 *K*, and 369.3 *K*. Because of the increase in the number of fins, the heat transfer rate increased leading to the surface temperature decrease. Also the effect of changing the velocity flow rate on the thermal effectiveness has been studied. The coefficient of convective heat transfer is observed to increased when the velocity flow rate increased that was because of the increasing of the heat removal rate.

Omojaro et al. [28] done an empirical study of single-pass and double-pass *SAH* with longitudinal fins' thermal effectiveness, all sides and bottom surface are insulated to prevent energy losses, the study is done for the effect of variation of the mass flow rate between 12×10^{-3} *kg/s*, and 38×10^{-3} *kg/s* on the thermal efficiency. The results showed that the double pass has higher thermal efficiency than the single pass by 7% - 19%, the higher efficiency occurred with the higher mass flow rate. Adding longitadunal fins has improved the thermal capacity by boost the thermal energy loss from the upper glass because fins are touching the upper glass.

Kumar Goel et al. [29] studied the frictional properties and thermohydraulic adequacy of an impingement air jet with the finned type of *SAH*, they found that the efficiency increases when the Reynolds number increases due to the incrament in cooling system.

Nayak et al. [30] worked on experiential research of the effectiveness of the *SAH* with a jet plate and longitudinal fins under crossflow and non-crossflow conditions, they found that the heat transfer was improved when added fins to the *SAH*. Also, the higher efficiency of the *SAH* was obtained with the crossflow condition than the non-cross flow because of the mixing of the two air flows.

Goel et al. [31] studied the *SAH* including jet plate and continuos longitidunal fins with Reynolds number between 3000 and 15000 and variation of the fin spacing, the

effective heat transfer coefficient has been increased when the *Re* number increased that means better heat transfer rate and higher efficiency. Also, the higher efficiency value (61 %) attained with a lower value of fin gap of 0.01 *m* and higher Reynolds number of 15000.

1.4. OBJECTIVE AND AIM OF THE STUDY

The fundamental objective of this study is to elucidate the unique contributions and novel advancements facilitated by experimental investigations, spearheaded by Chauhan and Thakur [38], within the domain of solar air heating systems. The study's aim is to discern and characterize the unexplored dimensions of solar air heater (*SAH*) efficiency enhancement through the implementation of impinging jets and longitudinally finned architectures. This pursuit ultimately seeks to redefine our understanding of *SAH* thermal dynamics, fostering innovative insights into the realms of enhanced convective heat transfer, elevated thermal efficiency, and amplified Nusselt numbers. The benefit of the *SAH* with impingement jets and fins is the simplicity of the system that leads to lower the cost. This research aims to investigate the influence of impingement jets on the lowering of the temperature of a *SAH* employing longitudinal fins, and then do a comparison of different shapes of fins, and then do a comparison of different shapes of fins. The study aims to numerically analyze the heat transfer rate and fluid flow properties of the system by applying *CFD* simulations.

The specific aims of the study include:

1. Investigating the influence of various shapes of longitudinal fins on the heat transfered capacity of the *SAH*.
2. Analyzing the impact of the impinging jet on the cooling of the *SAH*.
3. Determining the optimal designing specifications of the *SAH* with impinging jet cooling and longitudinal fins to achieve maximum heat transfer efficiency.
4. Providing insights into the underlying physics of the heat transfer and fluid flow mechanisms in the system.

5. Find the best dimension and geometry of the fins to improve the efficiency concurrently with decreasing pressure drop.

The findings of this study may contribute to the expansion of more efficient solar air heaters with impinging jet cooling and different shapes of longitudinal fins, which can have practical applications in the fields of renewable energy and sustainable building design.

PART 2

METHODOLOGY

The methodology employed in this thesis is founded upon a systematic and rigorous approach designed to investigate the complex interplay between impinging jet cooling and diverse longitudinal fin configurations in *SAH*s. Figure 2.1 presents the numerical analysis methodology chart.

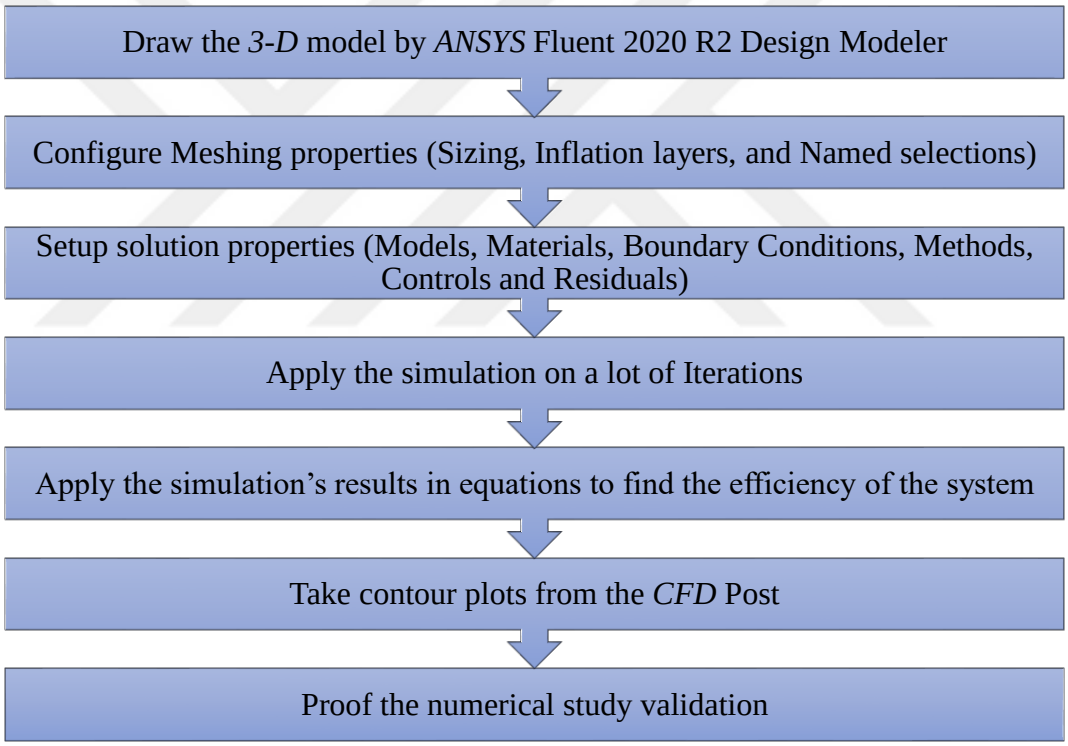

Figure 2.1. Numerical analysis methodology chart

2.1. PROBLEM DESCRIPTION

Numerical analysis has been used to determine how an impinging jet impacts a *SAH* efficiency with applying a different simulation cases. Also, for each case different shape of longitudinal fins have been attached on the absorber plate of the *SAH*. An absorber plate, a glass cover, two ducts through which the air passes, and impinging

jets between the ducts to boost air velocity are the typical components. A device called a solar air heater uses solar energy to warm air for a variety of purposes.

In solar air heaters, longitudinal fins are frequently employed to improve heat transfer and boost system effectiveness. It is crucial to research how different fin shapes affect the execution of the *SAH* because the design of the fins will considerably alter the system's heat transfer capabilities. Along with concentrating on analyzing the impact of the air impinged on the *SAH's* cooling. The feature that used to achieve a high velocity fluid that pumped directly to the surface of the *SAH* is named as impinging jet. Impinging jets are used to boost the thermal energy transmittion rate between the working fluid and the high temperature walls by cooling of the solar air heater.

In this study, *CFD* simulation is used to model the impinging jets and the air flow through the *SAH*, in additional to researching the influence of the different shapes of the fins on the efficiency of the system. Finaly, the results of the simulation are specifying the thermal efficiency of the designed project and approve the leverages of the impingment jets and longitudanal fins on the improvements of the heat transfer rate and efficiency.

2.1.1. *SAH* With Impinging Jets

Solidworks 2020 software has been used to draw the *2D* sketch and *3D* shape of the *SAH* just to describe the dimensions of it clearly. The dimensions and shape of the conventional *SAH* are described in Figure 2.2, Figure 2.3, and Table 2.1. After choosing the XZ plane of drawing the *2D* sketch has been extruded to get the model then impinging jets have been achieved by do the linear pattern with specifying the directions of pattern and number of bodies (Figure 2.2, Figure 2.3, and Figure 2.4). For analysis, *ANSYS* Fluent 2020 R2 was used firstly for modelling the *3D* computational domain, then meshing and applying the calculations to take the results.

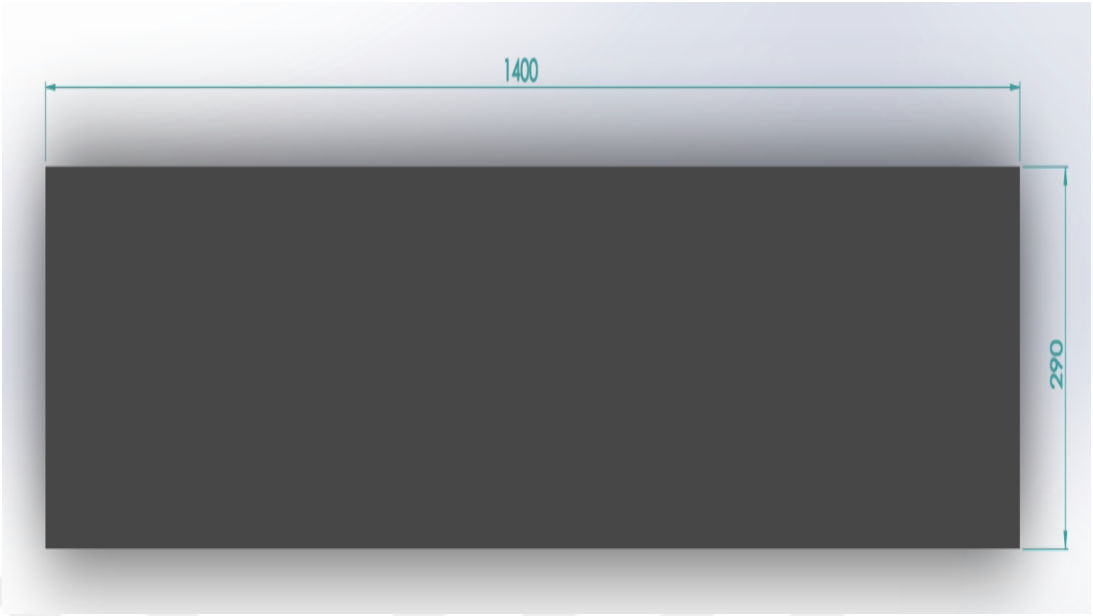

Figure 2.2. *SAH* length and width dimensions

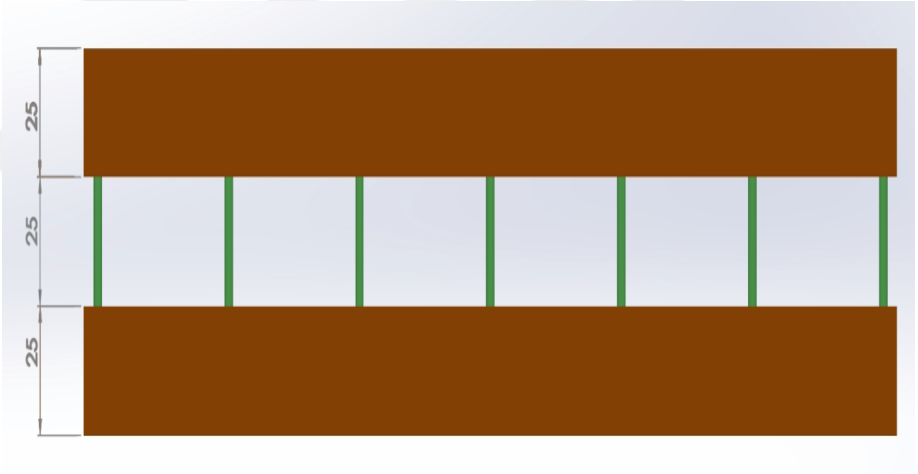

Figure 2.3. *SAH* height dimension

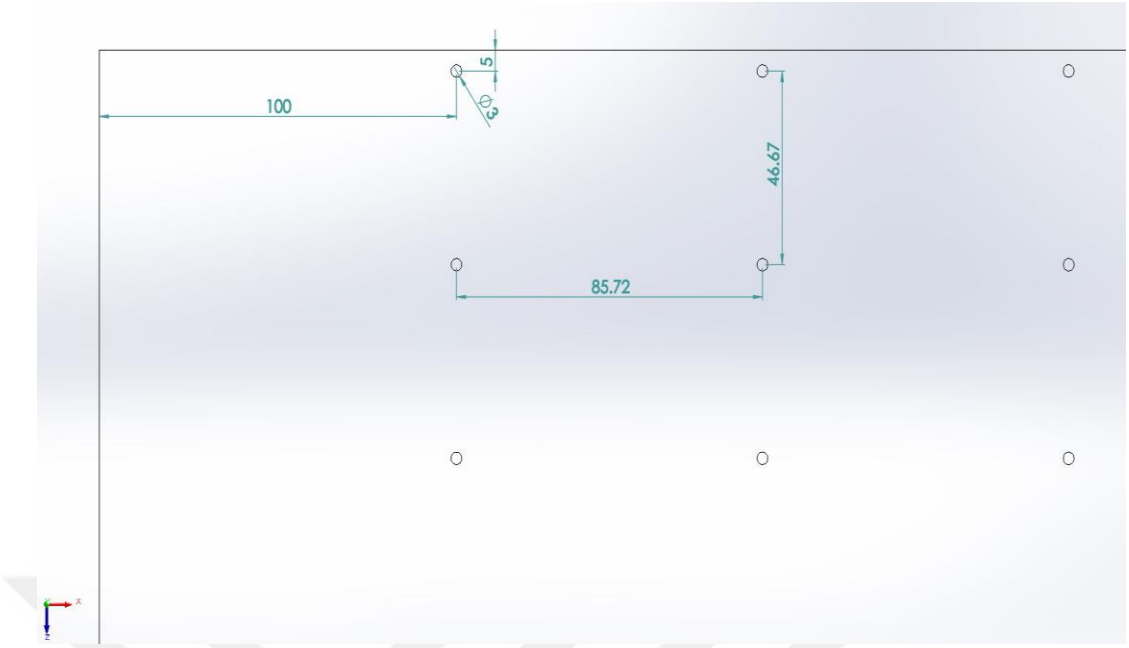

Figure 2.4. Jet locations and dimensions

Table 2.1. Dimensions of *SAH* with impinging jets [1].

Collector Length	1400 *mm*
Collector Width	290 *mm*
Collector Height	25 *mm*
Collector Hydraulic Diameter (D_h)	46.031 *mm*
Number of Glass Covers	1
Streamwise (X-direction) Number of Jets	15
Streamwise (X-direction) Center-to-Center Distance between each Jet	85.72 *mm*
Spanwise (Z-direction) Number of Jets	7
Spanwise (Z-direction) Center-to-Center Distance between each Jet	46.66 *mm*
Total Number of Impinging Jets	105
Impinging Jet Diameter (D_j)	3 *mm*

2.1.2. Finned *SAH* with Impinging Jets

The *2D* views and dimensions of fins are given in Figure 2.5, Figure 2.6, Figure 2.7, and Table 2.2, respectively. Also, the whole *3D* model of the *SAH* with fins and impinging jets are shown in Figure 2.8. In modelling the design, firstly the conventional *SAH* is drawn on the *XZ* plane and the fins are added and extruded to take a variable height to make the study on the fin's altitude.

Three different fin shape (rectangular, circular, and triangular) and four different fin heights (1.25 *mm*, 2.5 *mm*, 3.75 *mm*, and 5 *mm*) are used in the calculations to determine the best fin shape and dimension given highest thermal efficiency.

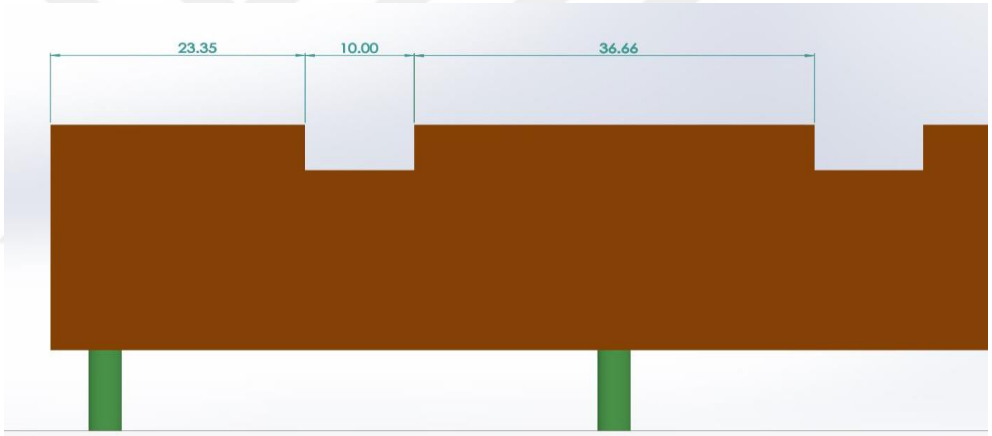

Figure 2.5. Dimensions of the rectangular fins.

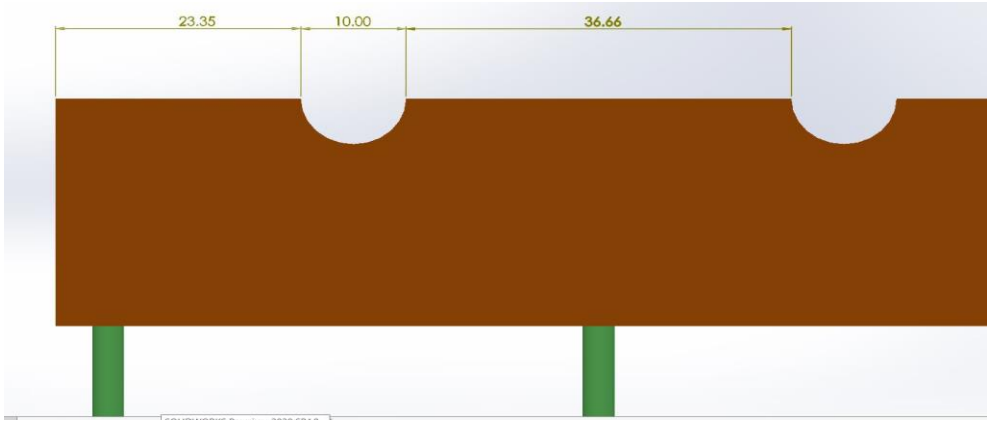

Figure 2.6. Dimensions of the circular fins.

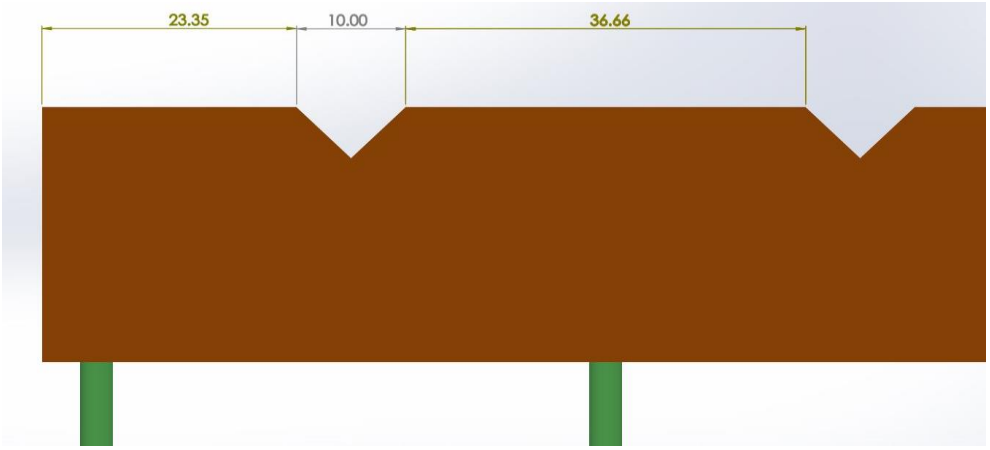

Figure 2.7. Dimensions of the triangular fins.

Table 2.2. Dimensions of fins [1].

Number of Longitudinal Fins	6
Fin Length (*L*)	1400 *mm*
Fin Thickness (*W*)	10 *mm*
Fin Height (*H*)	Variating between (1.25 *mm*, 2.5 *mm*, 3.75 *mm*, and 5 *mm*)

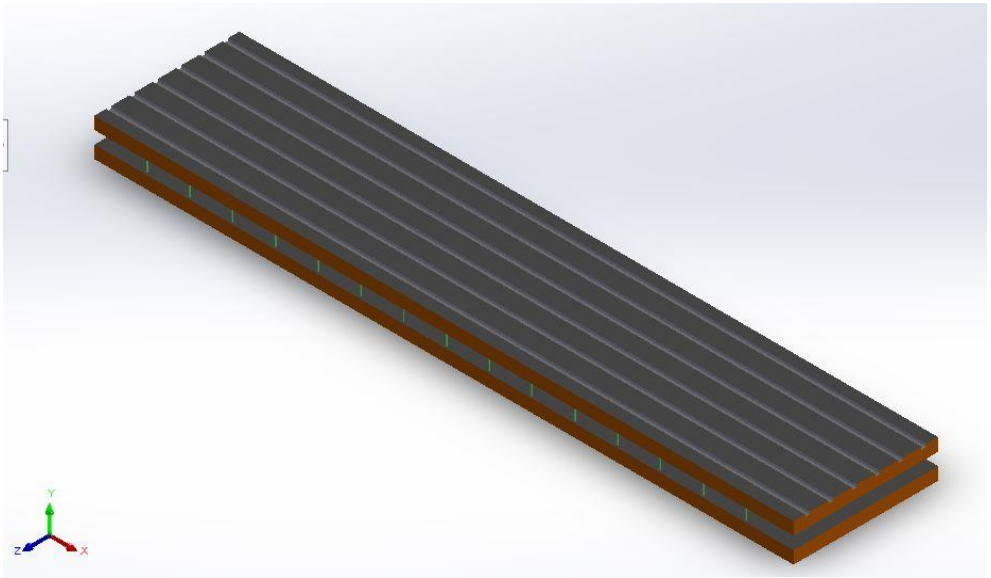

Figure 2.8. *3D* model view of the *SAH* with impinging jets and longitudinal fins.

2.2. ASSUMPTIONS AND CONSTANTS

2.2.1. Assumptions

Assumptions used in the numerical calculations are given below:

- Steady Flow.
- Air properties are constants and used as an incomprissible fluid.
- The system is analyzed under turbulent flow condition.
- Radiation heat transfer is neglected.
- Heat flux that applied on the absober plate is taken constant as 800 W/m^2.

2.2.2. Constants

The constants used in the numerical calculations are presented in Table 2.3.

Table 2.3. The constants used in the study [1].

Constant	Symbol	Value
Transmittance–Absorptance	$\tau\alpha$	0.8
Ambient Temperature	T_a	300 K
Emissivity of the Plate	ε_p	0.9
Emissivity of the Glass Cover	ε_g	0.88
Jet Diameter-Ratio	$\frac{D_j}{D_h}$	0.065
Streamwise Pitch Ratio	$\frac{X}{D_h}$	1.862
Spanwise Pitch Ratio	$\frac{Y}{D_h}$	1.01366
Stefan-Boltzman Constant	σ	5.67×10^{-8} $W/m^2.K^4$
Wind Velocity	V_w	1 m/s

2.3. THERMOPHYSICAL PROPERTIES

Air has been used as working fluid at *T=300 K* and *P=1 atm*. The walls of the *SAH* have been made of Aluminum. The properties of the Aluminum are also taken at *T=300 K*. The thermophysical properties of the air and aluminum are presented in Table 2.4.

Table 2.4. Thermophysical properties of the Air and Aluminum used in this study [32].

Property	Air	Aluminum
Density [kg/m^3]	1.1774	2719
Specific Heat [$J/kg.K$]	1007	871
Thermal Conductivity [$W/m.K$]	0.02565	202.4
Kinematic Viscosity [m^2/s]	1.569×10^{-5}	—

2.4. GOVERNING EQUATIONS AND BOUNDARY CONDITIONS

In this section of the thesis, governing and turbulence equations which they are solved in the numerical calculations, and system boundary conditions are presented in detail.

2.4.1. Governing Equations [1]

Continuity Equation [1]:

$$\frac{\partial \rho}{\partial t} + \frac{\partial (\rho u_i)}{\partial x} = 0 \tag{2.1}$$

Where *t* [*s*] represents time, and *u* [*m/s*] is the velocity component of the fluid.

Momentum Equation [1]:

$$\frac{\partial(\rho u_i)}{\partial t} + \frac{\partial\left(\rho u_i\, u_j\right)}{\partial x_j} = -\frac{\partial P}{\partial x_i} + \frac{\partial}{\partial x_j}\left[\mu\left(\frac{\partial u_i}{\partial x_j} + \frac{\partial u_j}{\partial x_i} - \frac{2}{3}\,\delta_{ij}\,\frac{\partial u_i}{\partial x_j}\right)\right] + \frac{\partial(\rho u_i)}{\partial t} + i\,\frac{\partial}{\partial x_j}\left(-\rho\,\overline{u_i u_j}\right) \quad (2.2)$$

Where P [Pa] is pressure, μ [$kg/m.s$] is the fluid dynamic viscosity, and ρ [kg/m^3] is fluid's density.

Energy Equation [1]:

$$\frac{\partial}{\partial t}(\rho E) + \frac{\partial}{\partial x_i}[\mu_i\,(\rho E + P)] = \frac{\partial}{\partial x_j}\left(k + \frac{C\mu_i}{Pr_t}\right)\frac{\partial T}{\partial x_j} + \mu_i\left(\tau_{ij}\right)_{eff} \quad (2.3)$$

Where T [K] is the fluid's temperature at a specific location, Pr is the Prandtl number of the fluid, E [J] is the internal energy, k [$W/m.K$] is the thermal conductivity, and τ_{ij} [Pa] is the viscous stress tensor components.

2.4.2. *SST k-ω* Turbulence Model Equations

The *Shear Stress Transport (SST) k-ω* turbulence model is a good option for studying the impacts of the impingement jets on the lowering temperatures performance of the *SAH* with attaching longitudinal fins because it is capable of properly predicting the flow characteristics in the near-wall and outer areas of the flow [33]. As key elements in effectively simulating turbulent flows, turbulent viscosity and Reynolds stress can also be considered. In this kind of investigation, the *SST k-ω* turbulence model is employed because impinging jets can result in complicated flow patterns that are frequently challenging to anticipate with accuracy using conventional turbulence models. The k and ω equations are given in Eq. (2.4), and Eq. (2.5) [33].

$$\frac{\partial}{\partial t}(\rho k) + \frac{\partial}{\partial x_i}(\rho k u_i) = \frac{\partial}{\partial x_j}\left[\left(\Gamma_k \frac{\partial k}{\partial x_i}\right)\right] + \tilde{G}_k - Y_k + S_k \quad (2.4)$$

$$\frac{\partial}{\partial t}(\rho \omega) + \frac{\partial}{\partial x_i}(\rho \omega u_i) = \frac{\partial}{\partial x_j}\left[\left(\Gamma_\omega \frac{\partial \omega}{\partial x_j}\right)\right] + G_\omega - Y_\omega + D_\omega + S_\omega \quad (2.5)$$

Where :

$\tilde{G}_k$: Generation of the turbulent kinetic energy (k) due to mean velocity gradients.

Y_k: Dissipation rate of kinetic energy (k) caused by the turbulence.

ω : Specific dissipation rate.

S_k *and* S_ω: User-define source terms.

G_ω: Generation of specific dissipation rate (ω).

Y_ω: Dissipation rate of ω caused by the turbulence.

D_ω: Cross-diffusion term.

2.4.3. Boundary Conditions

The system boundary conditions used in the calculations are presented in Table 2.5.

Table 2.5. System boundary conditions.

Boundary	Type	Option	Value
Inlet	Velocity-inlet	Momentum	V_{in}=variable with *Re* (3.41, 5.11, 6.82, and 8.52) [*m/s*]
			Turbulence specification method is set as Intensity and Hydraulic diameter

		Thermal	T_{in}=300 K
Outlet	Pressure-outlet	Momentum	Gauge Pressure=0
			Turbulence specification method is set as Intensity and Hydraulic diameter
Heated Wall	Wall	Momentum	• Stationary wall • No slip shear condition • Standard roughness model with a roughness constant=0.5
		Thermal	Heat flux (q'' =800 W/m^2)
Adiabatic Wall	Wall	Momentum	• Stationary wall • No slip shear condition • Standard roughness model with a roughness constant=0.5
Symmetry	Symmetry	-	-

2.4.4. Reynolds Number

The Reynolds number represents the ratio of inertial to viscous forces. It is a dimensionless parameter employed to classify fluid systems, and viscosity plays a significant role in taking control of velocities or the flow pattern of a fluid, it represents the fluid's flow type if it is laminar or turbulent [34]. Reynolds number is expressed in Eq. (2.6) [12].

$$Re = \frac{V_{in} \times D_h}{\nu} \tag{2.6}$$

Where V_{in} [m/s] is the average velocity, v [m^2/s] is the kinematic viscosity of the fluid, and D_h [m] is the hydraulic diameter that expressed below in Eq. (2.7) [12].

$$D_h = \frac{4A}{P} \tag{2.7}$$

Where A [m^2] is the cross-sectional area, and P [m] is the perimeter of the duct.

2.4.5. Turbulence Intensity

Turbulence intensity is calculated by using Eq. (2.8) [1], then it is used in boundary conditions.

$$I_{turbulent\ intensity} = 0.16\ Re^{-\frac{1}{8}} \tag{2.8}$$

2.4.6. Nusselt Number

The Nusselt number is an important metric that describes the ratio of convection heat transfer to conduction heat transfer. It is also used to specify the type of heat transfer whether it is conduction or convection [35]. Nusselt number for the convection heat transfer that occurs in a rectangular duct is expressed in Eq. (2.9) [35].

$$Nu = \frac{h\,.\,D_h}{k} \tag{2.9}$$

Where k [$W/m.\ K$] is the thermal conductivity of the working fluid, and h [$W/m^2.K$] is the average convection heat transfer coefficient that expressed in the Eq. (2.10) [1].

$$h = \frac{q''}{T_{pm} - T_b} \tag{2.10}$$

Where q'' [W/m^2], is the heat flux, T_{pm} [K] is the main surface temperature, and T_b [K] is the bulk temperature of the air.

2.4.7. Pressure Drop

Pressure drop is the pressure difference between the inlet and outlet of the system. It occurs due to many reasons such as friction, momentum, or diffusion [36]. The pressure drop is also known as a pressure loss. It is an essential factor that affects the system's efficiency because of directly proportional to the cost of pneumatic power. While the pressure drop is increasing, the cost of pumping power is also growing.

2.4.8. Total Plate Loss Coefficient

$$(U_L) = U_t + U_b \tag{2.11}$$

Where U_L $[W/m^2.K]$ is the total plate loss coefficient expressed in Eq. (2.11) [1], U_t $[W/m^2.K]$ is the top loss plate coefficient expressed in Eq. (2.12) [1], and U_b $[W/m^2.K]$ is the bottom loss plate coefficient evaluated in Eq. (2.17) [39].

$$U_t = \left[\frac{N}{\frac{C}{T_{pm}}\left[\frac{T_{pm}-T_a}{N+f}\right]^e} + \frac{1}{h_w}\right]^{-1} + \left[\frac{\sigma\left(T_{pm}+T_a\right)\left({T_{pm}}^2+T_a^2\right)}{\frac{1}{\varepsilon_p+0.00591\,.\,N\,.\,h_w}+\frac{2\,N+f\,-1+0.133\,\varepsilon_p}{\varepsilon_g}-N}\right] \tag{2.12}$$

Where *N* is the number of glass covers, T_a $[K]$ Ambient Temperature, σ $[W/m^2.K^4]$ is Stefan-Boltzman constant = 5.67×10^{-8}, ε_p is the emissivity of the plate, ε_g is the emissivity of the cover.

C, *f*, and *e* are empirical factors that are expressed in Eqs. (2.13), (2.14), and (2.15) [1].

$$C = 520 \times (1 - 0.000051\,\beta^2) \tag{2.13}$$

Where β is the collector degree. It is assumed to be as a constant value of 70º [1].

$$f = \left(1 + 0.089\ \mathrm{h_w} - 0.1166\ h_w\ \varepsilon_p \right) (1 + 0.07866\ N) \tag{2.14}$$

Where h_w $[W/m^2.K]$ is the wind heat transfer coefficient that expressed in Eq. (2.16) [1, 37].

$$e = 0.430 \left[1 - \frac{100}{T_{pm}} \right] \tag{2.15}$$

$$h_w = 5.7 + 3.8\ V_w \tag{2.16}$$

Where V_w $[m/s]$ is the wind velocity. Eq. (2.16) is applied to evaluate the heat transfer coefficient when $V_w \leq 5\ m/s$ [37].

$$U_b = \frac{k}{H} \tag{2.17}$$

Where H $[m]$ is the thickness of the bottom plate.

2.4.9. Useful Energy Gain

It is solved to take only the useful energy generated without any losses from top and bottom surfaces. The useful energy gain Q_u $[W]$ is expressed in Eq. (2.18) [1].

$$Q_u = A_p\ .\left[S - U_L\ \times \left(T_{pm} - T_a \right) \right] \tag{2.18}$$

Where A_p $[m^2]$ is the area of the absorbing plate, T_a $[K]$ is the ambient temperature, and S $[W/m^2]$ is the absorber solar radiation that expressed in the Eq. (2.19) [1].

$$S = \tau\alpha \times I \tag{2.19}$$

Where $\tau\alpha$ is the Transmittance–absorptance, and I $[W/m^2]$ is the solar radiation intensity.

2.4.10. Thermal Efficiency of the System

Thermal efficiency ($\acute{\eta}$) is used to discuss how much the system is efficient, and knows that the system is effective or not, thermal efficiency is expressed in Eq. (2.20) [39].

$$\acute{\eta} = \frac{Q_u}{I \,.\, A_p} \tag{2.20}$$

2.5. NUMERICAL MODEL

In this section, it is explained all of the steps following in the numerical calculations.

2.5.1. Geometry Modeling

Firstly, *2D* sketch for each part of the *SAH* has been designed, then it is extruded for determination *3D* design separately. In additional to make the rectangular pattern for the impinging jets to take their locations on the *SAH* using the dimensions given in Table 2.1. After finishing the study of the designing of *SAH* without fins, six longitudinal fins have been added into the geometry using the dimensions given in Table 2.2.

2.5.2. Mesh

After finishing drawing the model, mesh is the most important step for achieving more accurate results. Figure 2.9-Figure 2.11 show the mesh details. In this regard, the body sizing on the whole body and edge sizing for all edges have been used (Figure 2.9 and Figure 2.10). In addition to this step, the inflation layers on the walls have been done

for taking care to make the layers enlarging smoothly as shown in Figure 2.11 to be more efficient on the accuracy of the simulations.

In the mesh section, the named selection must be achieved to specify the parts of the system, the names of inlet, outlet, wall solid, wall heated, and symmetry have been given. Since the system has geometrically and thermally symmetrical, the symmetry section has been used and half of the computational domain has been solved.

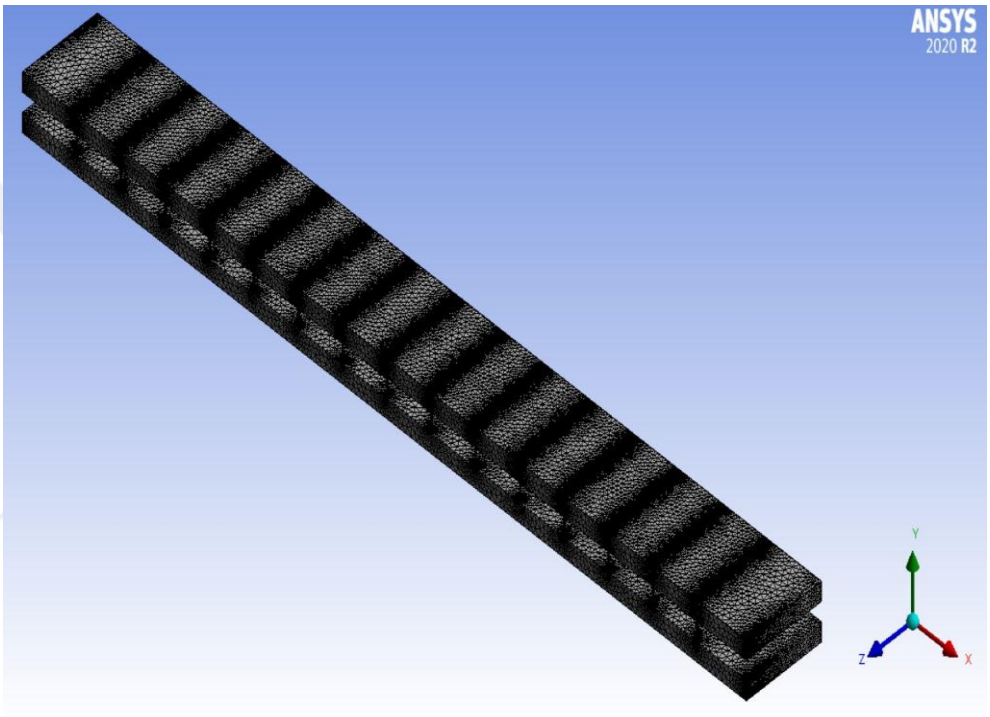

Figure 2.9. Smooth *SAH* Mesh.

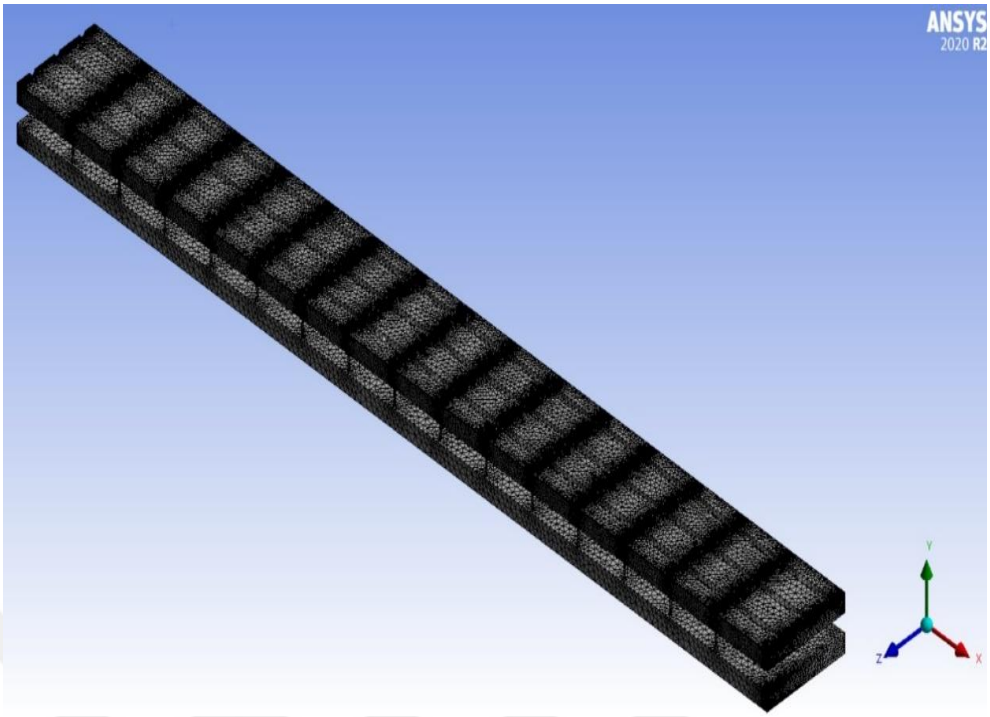

Figure 2.10. Finned *SAH* mesh.

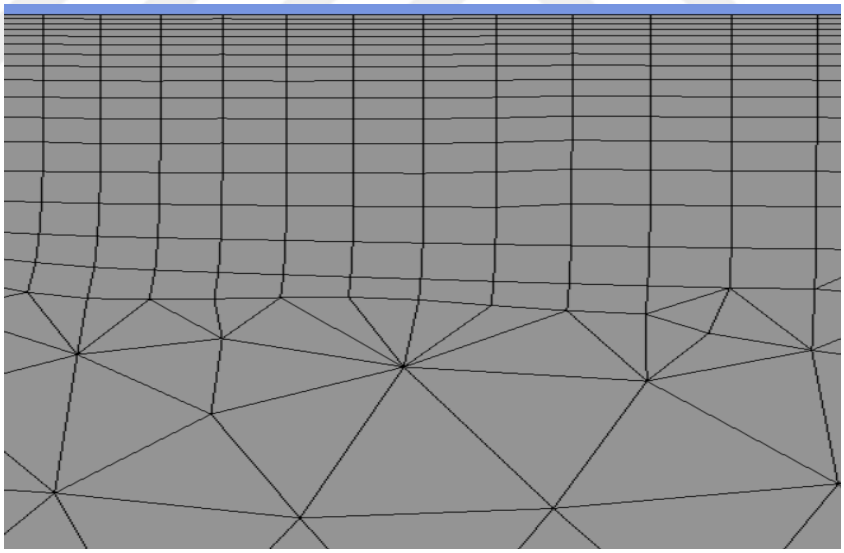

Figure 2.11. Inflation layers.

2.5.3. Models

1. Energy equation has been settled on.
2. *SST k-ω* turbulence model with its defaults configurations and constants has been used.

2.5.4. Methods

Because this investigation includes fluid-structure interaction, where the fluid flow impacts the temperature distribution in the solid fins, the Coupled technique in *ANSYS* Fluent should be employed. As a result, the interactions between the fluid and solid domains may be better represented, resulting in more accurate results. Furthermore, because of the research includes a variety of longitudinal fin designs it is critical to consider how geometry affects the results. The geometry of the fins might be brought into the analysis utilizing the Coupled method, resulting in more precise results. Because of the steady state, Pseudo-Transient is checked to improve the convergence of the solution [1]. The properties of solution methods are shown clearly in the Figure 2.12.

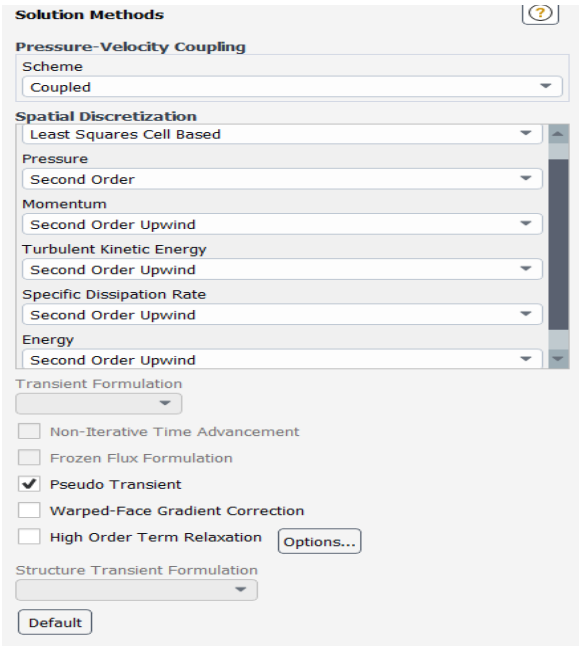

Figure 2.12. Solution methods properties [40].

2.5.5. Solution Controls

The Solution Controls for under relaxation factors using in the calculations are given in the Table 2.6 [40].

Table 2.6. Solution Controls for under relaxation factors [40].

Pressure	*0.5*
Momentum	*0.5*
Density	*1*
Body Forces	*1*
Turbulent Kinetic Energy	*0.75*
Specific Dissipation Rate	*0.75*
Turbulent Viscosity	*1*
Energy	*0.75*

2.5.6. Simulation Residuals

The residuals are set varied according to the ability of convergence for each other (Figure 2.13 and Figure 2.14):

- k and ω have been set to 0.001.
- Continuity, x-velocity, y-velocity, and z-velocity have been set to 0.0001.
- Energy has been set to 10^{-6}.

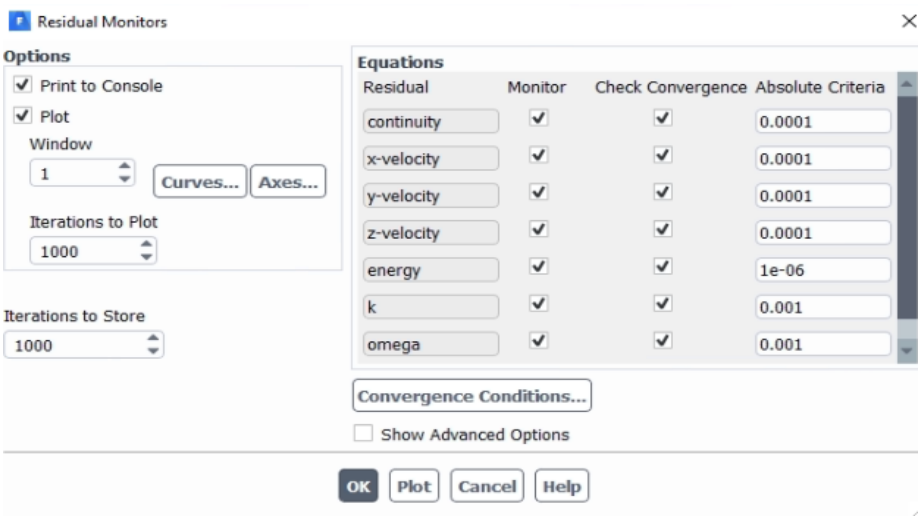

Figure 2.13. Residuals values [40].

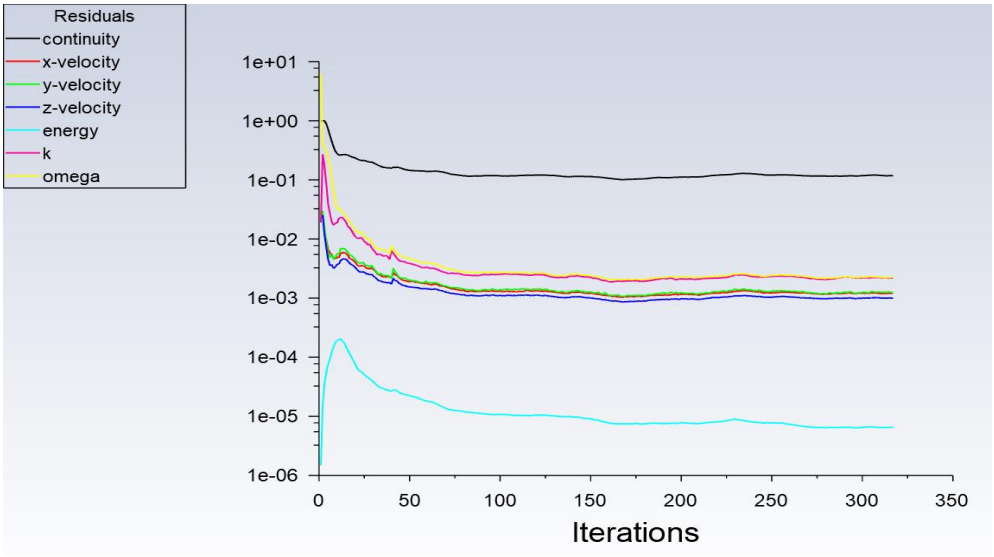

Figure 2.14. Residuals with iterations.

2.5.7. Initialization

A hybrid initialization has been applied for this simulation because a hybrid initialized solution is significantly more similar to the final converged solution than a conventional initialized solution.

2.6. NUMERICAL STUDY VALIDATION

To ensure that the simulations of the study are correct and have acceptable results, the numerical results have been compared with an experimental study data by Chauhan and Thakur [38]. The percent error between the numerical simulations results and experimental data are given in Table 2.7. According to the Table 2.7, It was decided that the *CFD* simulation can be acceptable and verified with smoothly convergence results. Also, *SAH* efficiencies have been compared and the comparison is given in Figure 2.15. It is also seen that the numerical results are harmonies with experimental data. Percent error equation is expressed in Eq. (2.21).

$$\%\ Error = \left|\frac{Experimental\ Value - \ Theoretical\ Value}{Theoretical\ Value}\right| \times 100 \qquad (2.21)$$

Table 2.7. Percent error between the numerical simulations results and experimental data.

Reynolds Number	*Percent Error*
10000	*11.04 %*
15000	*5.24 %*
20000	*2.8 %*
25000	*1.2 %*

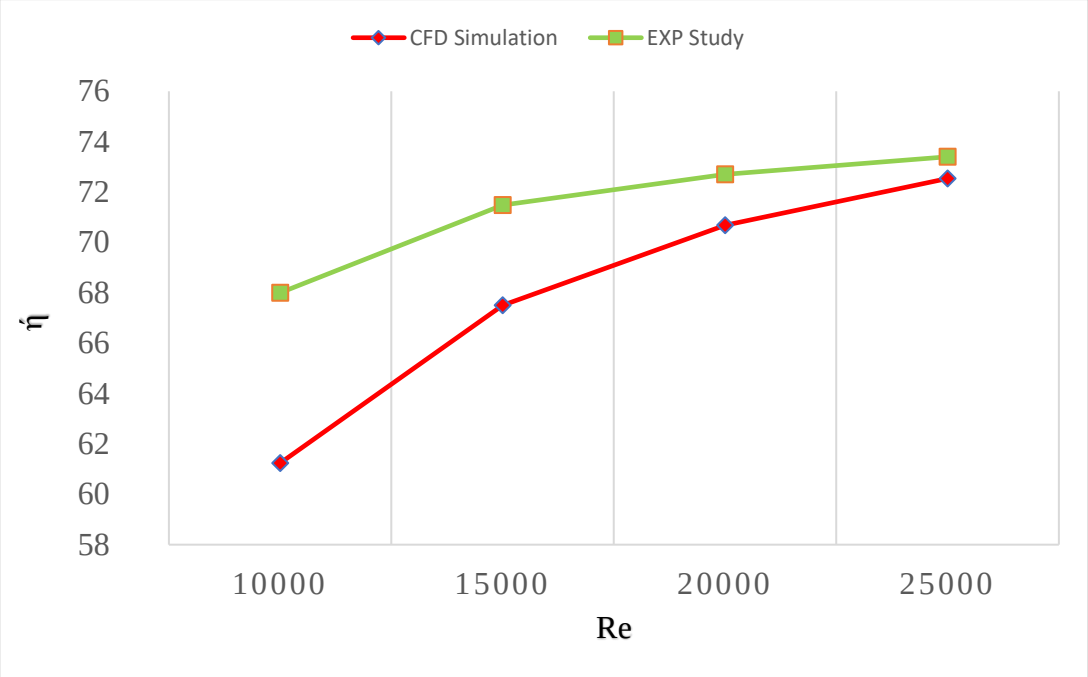

Figure 2.15. Numerical simulation results and experimental data [38].

Because of using *k-ω SST* turbulence model we should take attention on the near wall function (y^+) values to know that the mesh is validate and acceptable. y^+ values have been found between the range of 2.464 and 3.840 and this range can be accepted for this study [1].

PART 3

RESULTS AND DISCUSSIONS

In this part of the study, the findings of the simulation are expressed here to show how this study improves the efficiency of the system and the effects of adding and varying the fin height on increasing the system efficiency.

3.1. *SAH* SIMULATION

In the simulations, the main properties of this study are described as a values and locations of distribution on the *SAH* such as veloocity, pressure, and temperature distributions.

3.1.1. Velocity Vectors

As shown in the Figure 3.1 and Figure 3.2, the air enters the *SAH* with low velocity until it reaches impinging jets, then starts increasing because of the decreace in the cross-sectional area. As the air enters jets, the upper duct's velocity values gradually increase until the air exits the *SAH*. Additionally, Figure 3.3 shows that the velocity is lower near the walls in the lower duct. This is due to the friction force, which decreases the air's velocity.

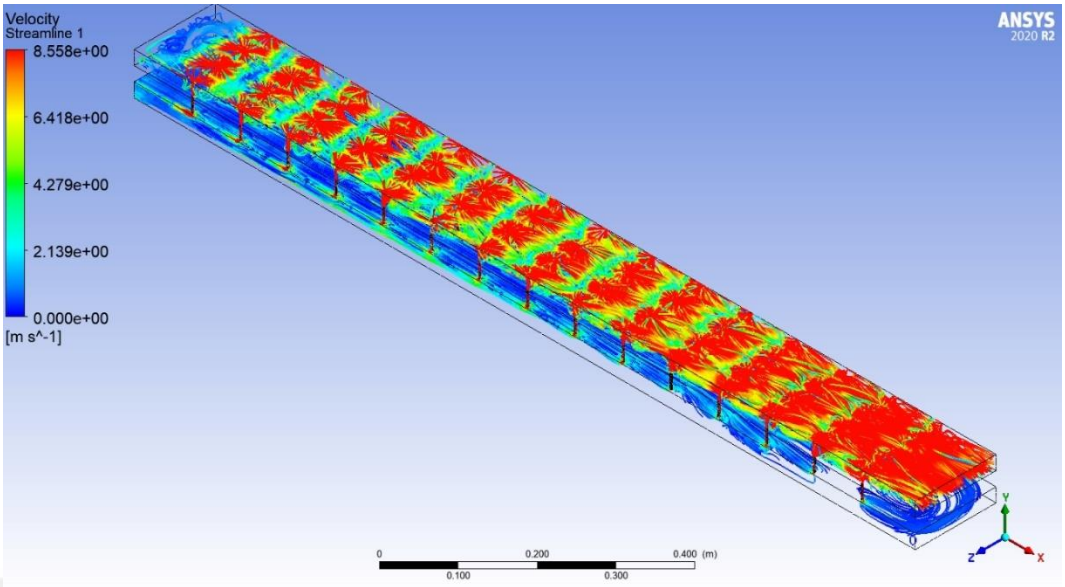

Figure 3.1. *3D* view of the velocity vector distribution.

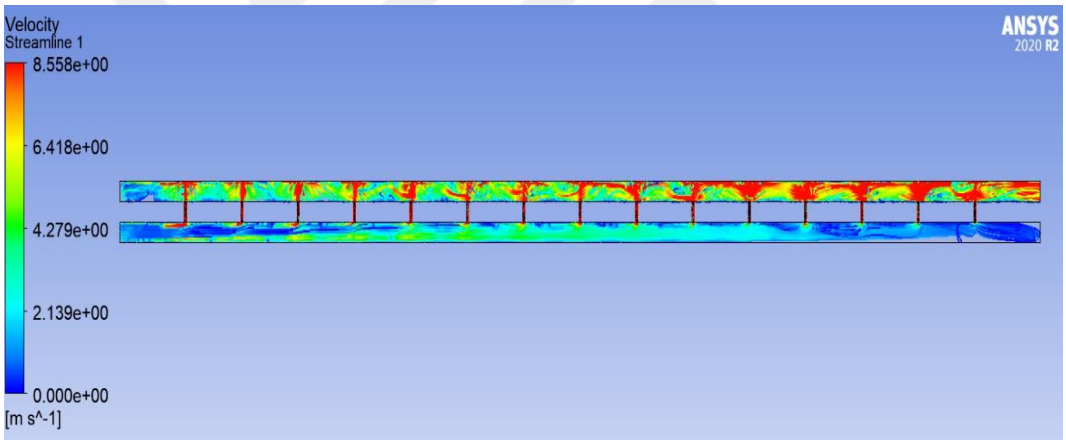

Figure 3.2. Side view (*XY* plane) of the velocity vector distribution.

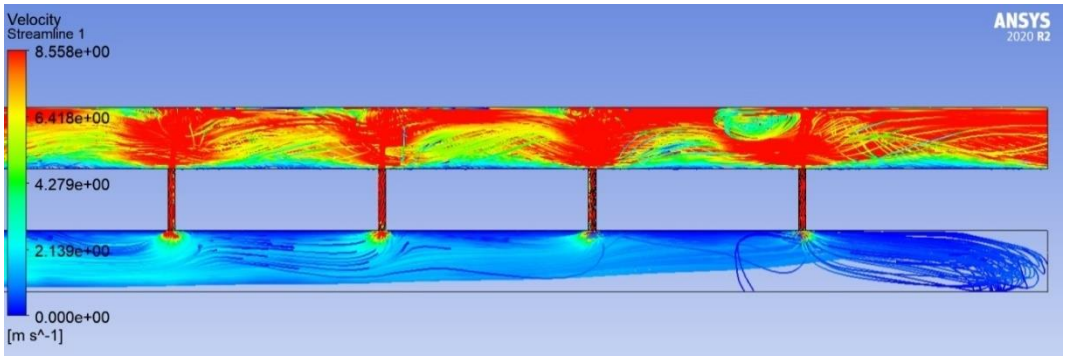

Figure 3.3. Velocity vector distribution through the impinging jets.

3.1.2. Temperature Distribution

3.1.2.1. Smooth Absorber Plate Surface Temperature Disribution

In the Figure 3.4-Figure 3.7, the temperature disribution is expressed for different Reynolds numbers to show where the temperature is distributed, and how the forced convection heat transfer occurs as a result of the air flowing by the impingment jets. The absorber plate surface temperature decreases when the air velocity increaces. It means that a better cooling occures by the forced heat transfer rate that leads to better efficiency by the increament of velocity.

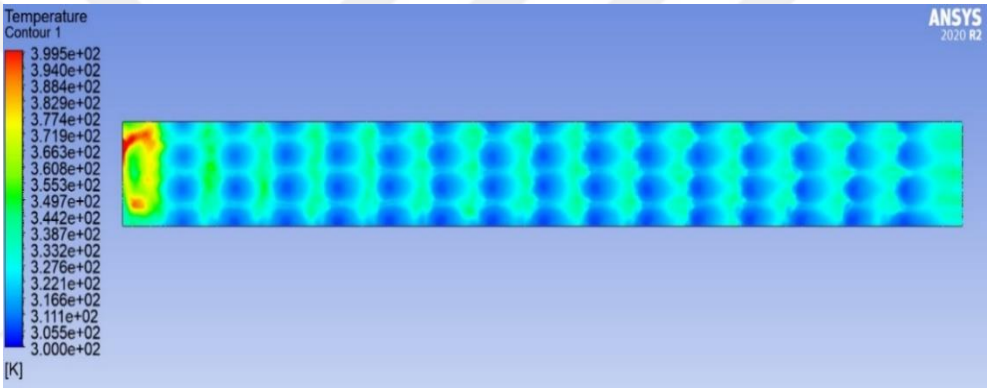

Figure 3.4. Temprature distribution on the absorber plate for Re=10000.

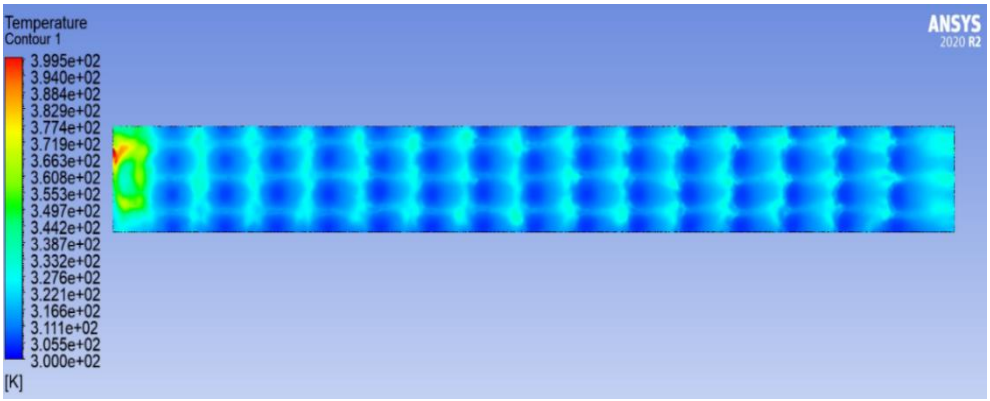

Figure 3.5. Temprature distribution on the absorber plate for Re=15000.

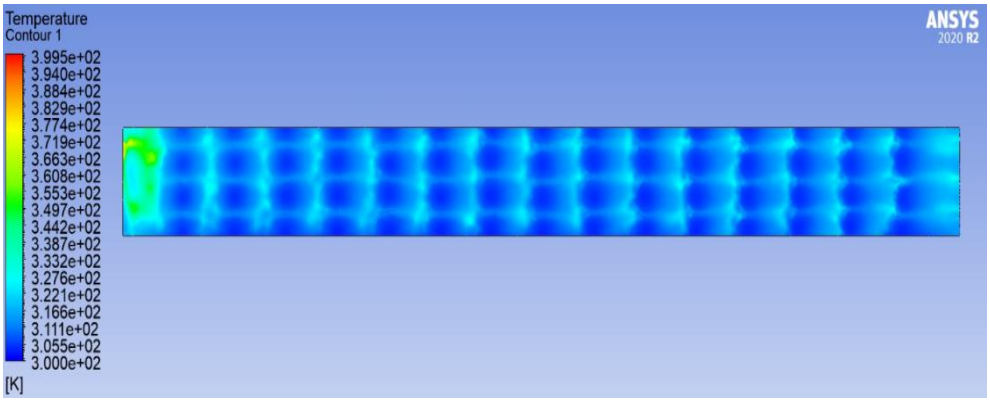

Figure 3.6. Temprature distribution on the absorber plate for Re=20000.

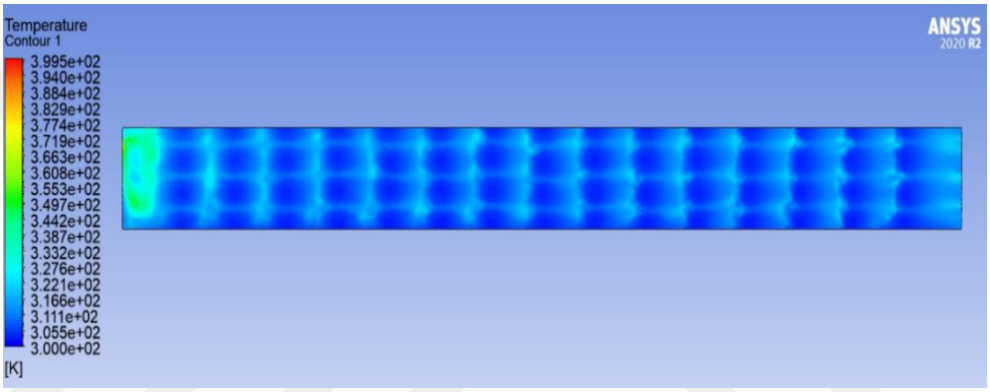

Figure 3.7. Temprature distribution on the absorber plate for Re=25000.

3.1.2.2. Finned Collector Surface Temperature Disribution

In Figure 3.8-Figure 3.11, temperature distributions on the absorber plate surface of the finned *SAH* with impinging jets are presented. The effects of the fins in cooling the collector surface are seen clearly in these figures. When adding the fins to the *SAH* with impinging jets the temperature distribution changes to show less surface temperature than smooth absorber plate surface. Since the increment in heat transfer surface area, better thermal efficiency is achived in this system.

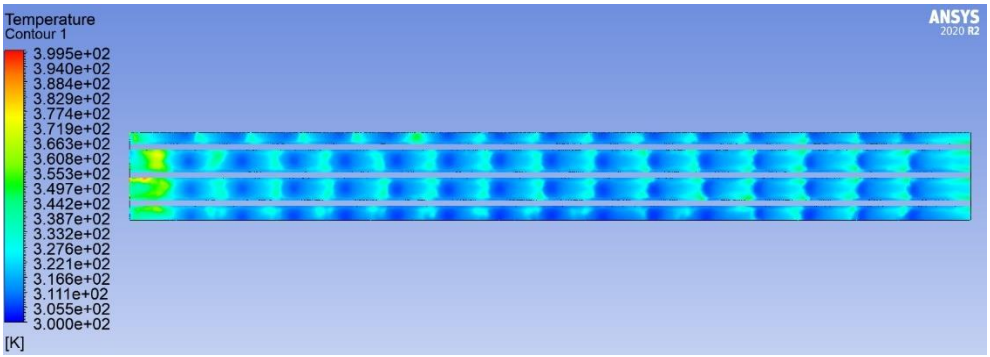

Figure 3.8. Temprature distribution on the absorber plate with fins for Re=10000.

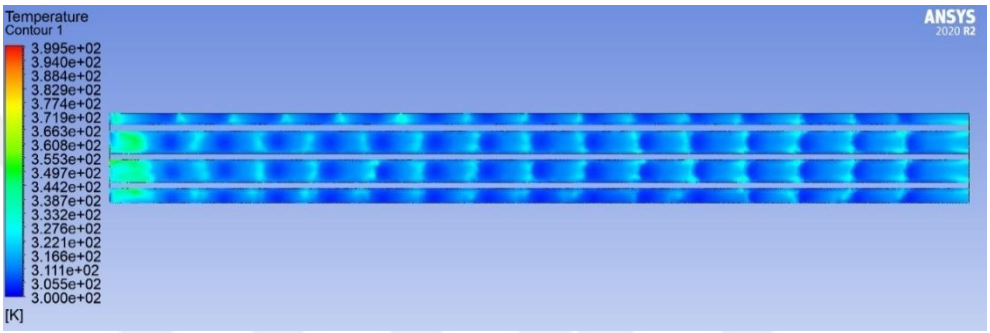

Figure 3.9. Temprature distribution on the absorber plate with fins for Re=15000.

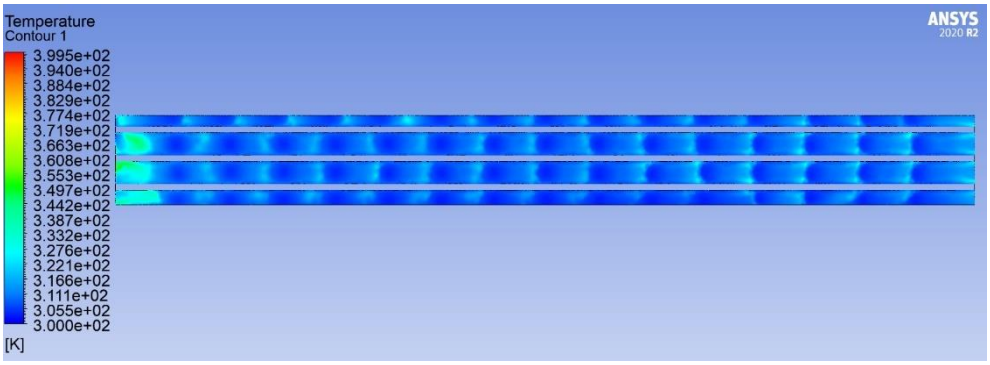

Figure 3.10. Temprature distribution on the absorber plate with fins for Re=20000.

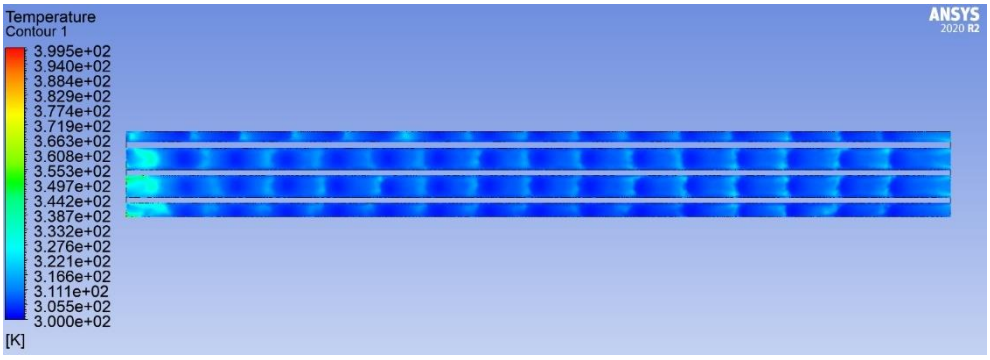

Figure 3.11. Temprature distribution on the absorber plate with fins for Re=25000.

3.1.3. Nusselt Number Distribution

3.1.3.1. Smooth Collector Surface Nusselt Number Distribution

In the Figure 3.12-Figure 3.15, the Nusselt number disribution is expressed for different Reynolds numbers to show that where the Nusselt number is distributed, and how the forced convection heat transfer occurs as a result of the air flowing by the impingment jets. The absorber plate surface Nusselt number increases when the air velocity increaces. It means that a better cooling occures by the forced heat transfer rate that leads to better efficiency by the increament of velocity. Nusselt number highly distributing at the points of of striking air on the absorber plate that means higher convection heat transfer occurs due to the impinging jet.

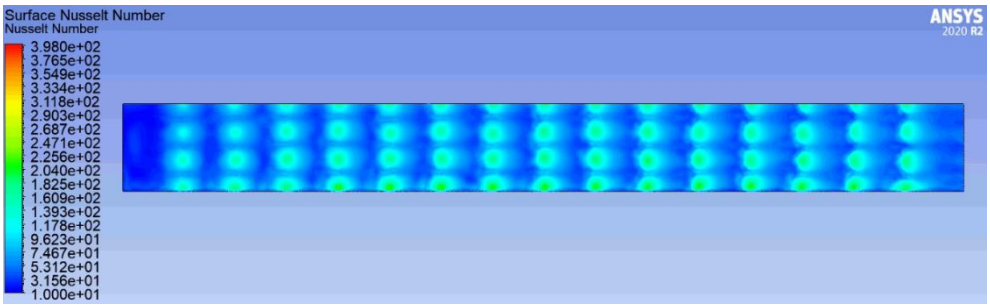

Figure 3.12. Nusselt Number distribution on the absorber plate for Re=10000.

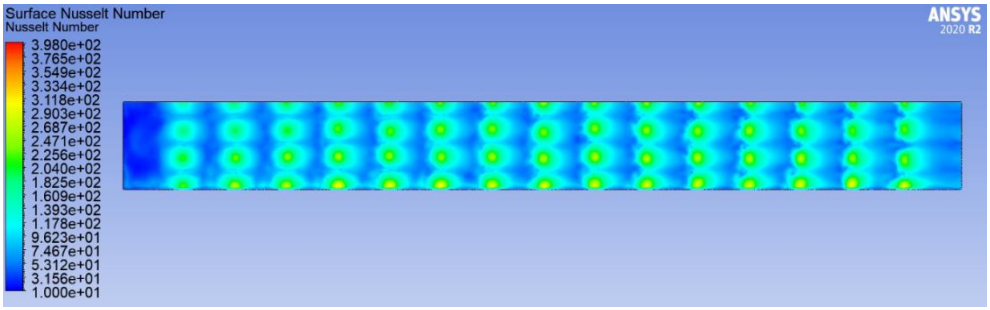

Figure 3.13. Nusselt Number distribution on the absorber plate for Re=15000.

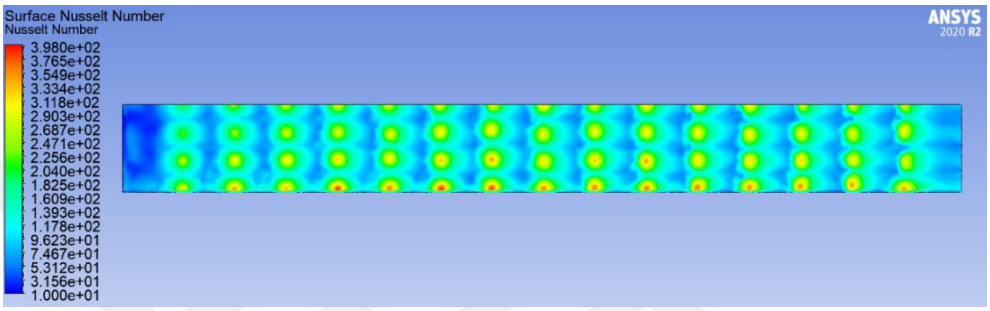

Figure 3.14. Nusselt Number distribution on the absorber plate for Re=20000.

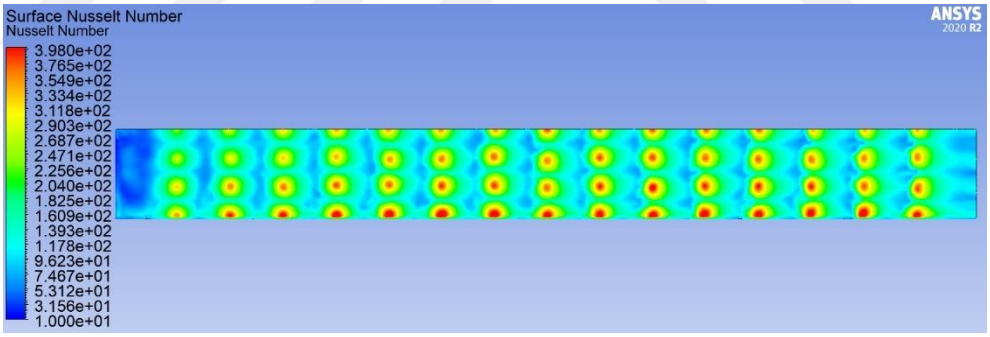

Figure 3.15. Nusselt Number distribution on the absorber plate for Re=25000.

3.1.3.2. Finned Collector Surface Nusselt Number Disribution

In Figure 3.16-Figure 3.19, Nusselt number distributions on the absorber plate surface of the finned *SAH* with impinging jets are presented. The effects of the fins in increasing the Nusselt number are seen clearly in these figures. When adding the fins to the *SAH* with impinging jets the Nusselt number distribution changes to show higher Nusselt number values than smooth absorber plate surface. Since the increment in heat

transfer surface area, better thermal efficiency is achived in this system due to higher Nusselt number hence an increase in the convection heat transfer rate.

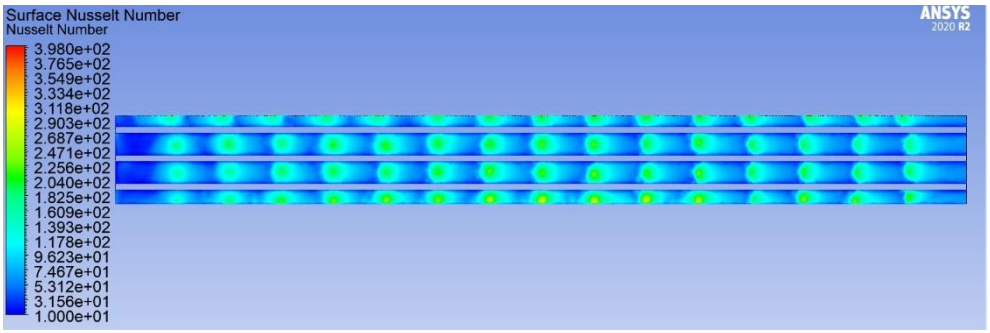

Figure 3.16. Nusselt Number distribution on the absorber plate with fins for Re=10000.

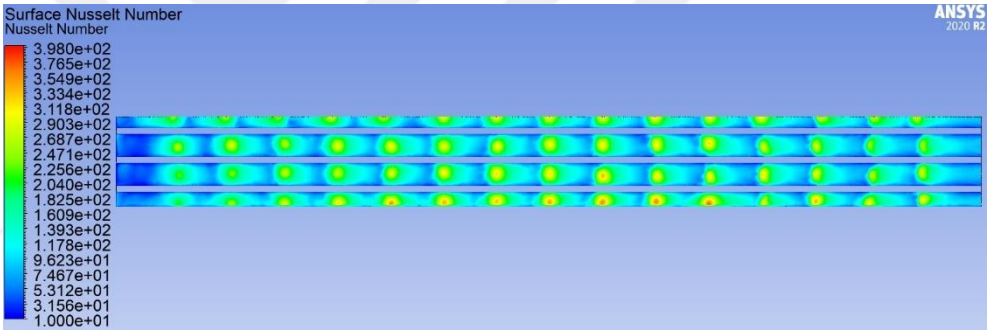

Figure 3.17. Nusselt Number distribution on the absorber plate with fins for Re=15000.

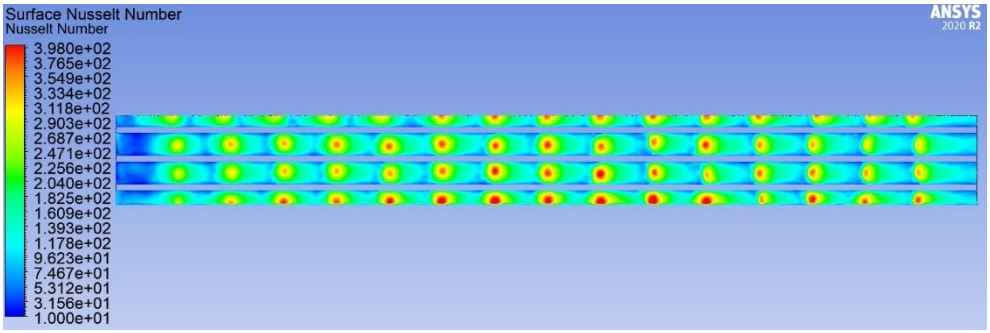

Figure 3.18. Nusselt Number distribution on the absorber plate with fins for Re=20000.

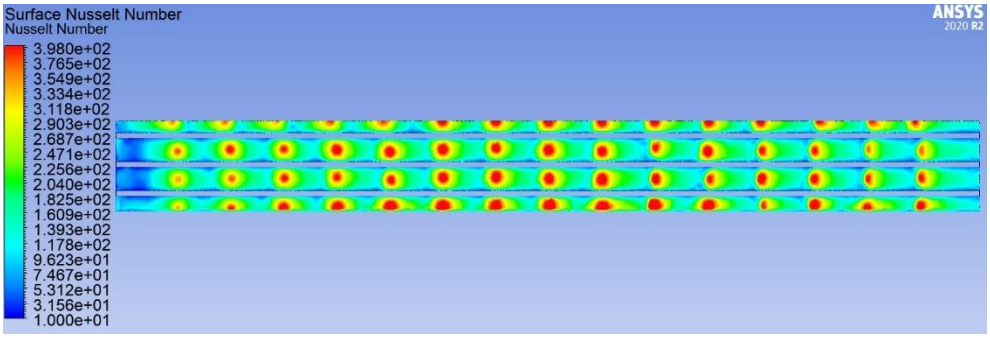

Figure 3.19. Nusselt Number distribution on the absorber plate with fins for Re=25000.

3.1.4. Pressure Distribution

3.1.4.1. Smooth Collector Surface Pressure Distribution

Pressure drop is one of the essential characteristics in heat transfer applications because it affects pneumatic power consumption and is inversely proportional to it. In Figure 3.20-Figure 3.22, the pressure distribution in the smooth collector is shown, in these figures, the pressure drop is seen as the pressure starts to decrease during the flow in jets due to the friction and viscous losses. Because of the loss of kinetic energy, the air's pressure decreases too much after it leaves the jets. Also, we notice that there is a higher pressure where the air is impinging directly on the inner collector surface than the other places.

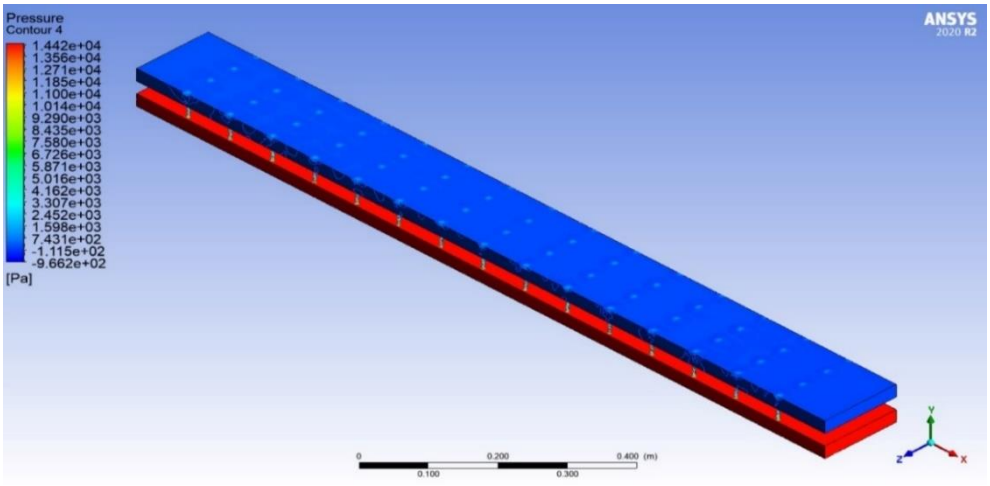

Figure 3.20. *3-D* view of pressure distribution on the smooth absorber.

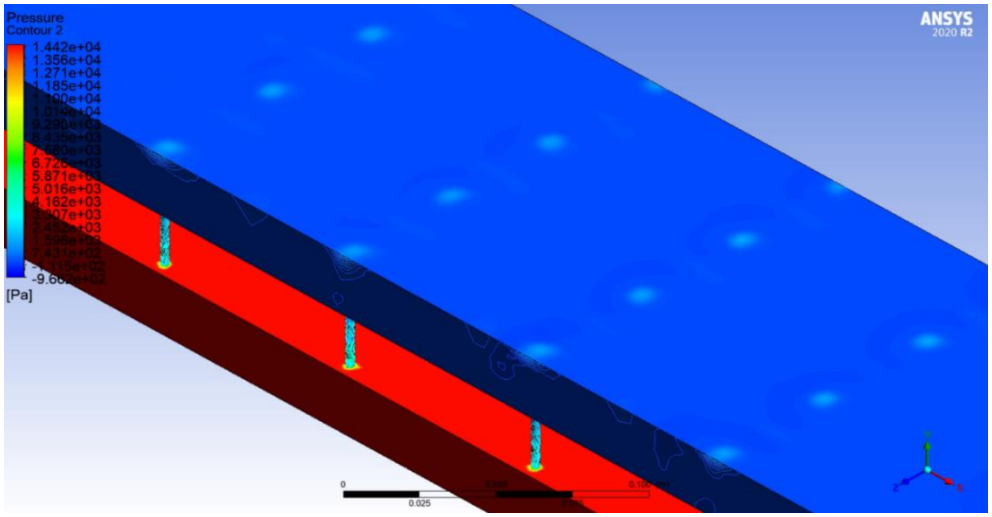

Figure 3.21. *3-D* zoomed-in view of pressure distribution on the smooth absorber.

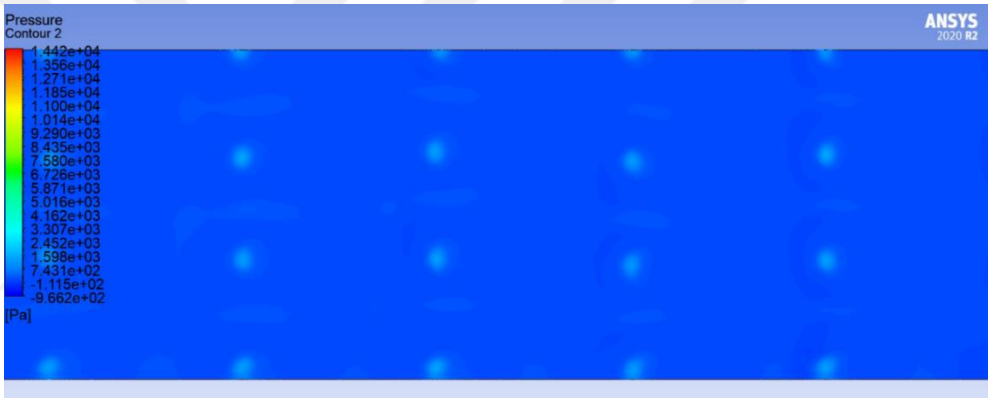

Figure 3.22. Top view of pressure distribution on the smooth absorber.

3.1.4.2. Finned Collector Surface Pressure Distribution

In Figure 3.23-Figure 3.25, it can be seen that the pressure distribution locations in the finned collector *SAH*. These are the same as the smooth collector but the values of the pressure at every location are higher than the smooth collector pressure values, the pressure drop of the finned *SAH* appears higher than the smooth *SAH*. This increase in pressure drop is caused by the increment of surface area which resulting more friction force between the working fluid and walls.

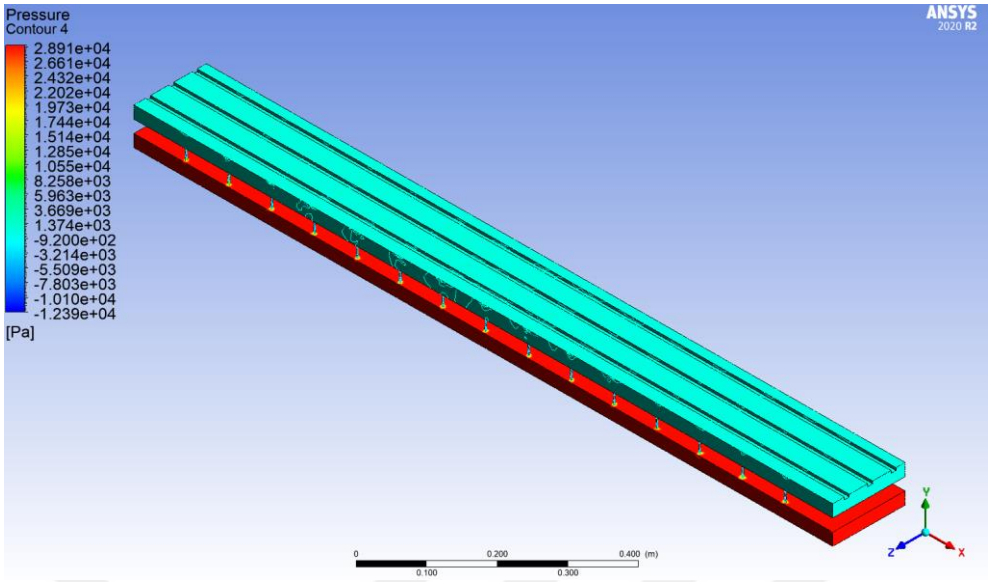

Figure 3.23. *3-D* view of pressure distribution on the finned absorber.

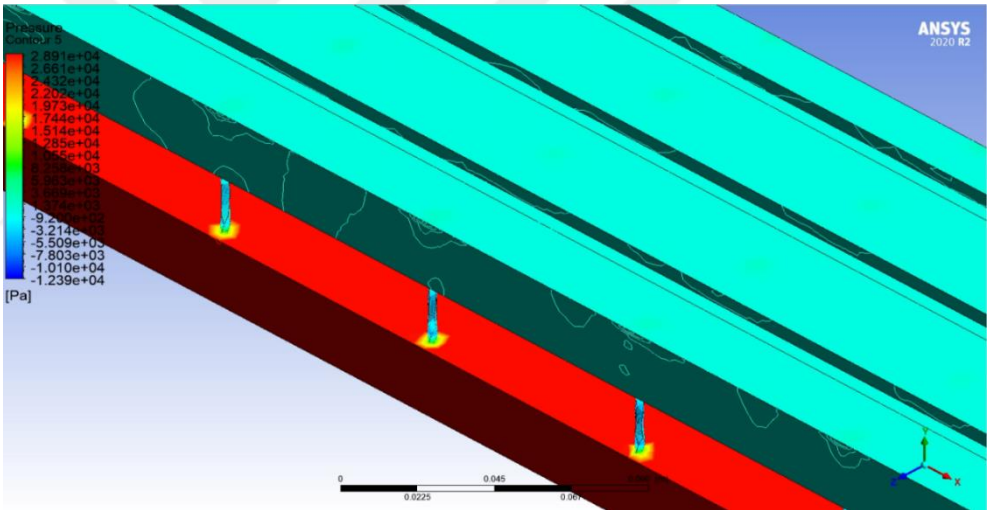

Figure 3.24. *3-D* zoomed-in view of pressure distribution on the finned absorber.

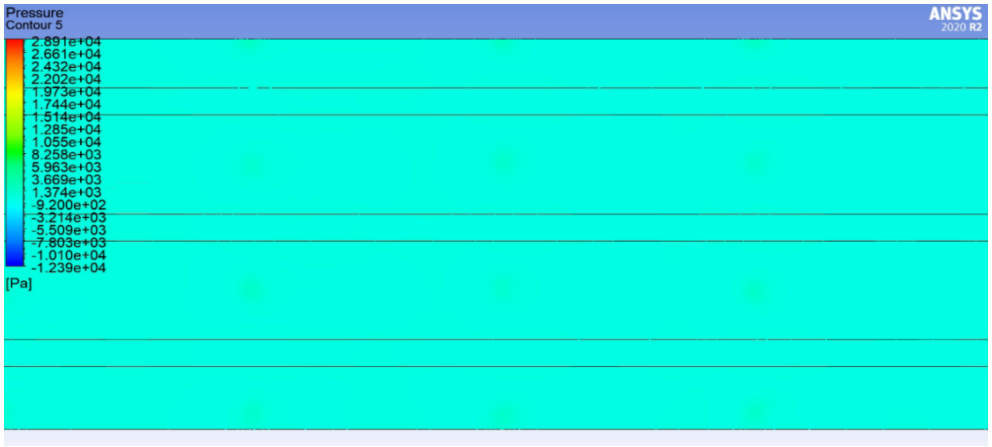

Figure 3.25. Top view of pressure distribution on the finned absorber.

3.2. PARAMETRIC STUDIES

In this section, it is combined all of the results with all parameters and variables giving the final discussion of the optimum fin shape and dimensions.

Table 3.1 presents the findings of the simulation on the *SAH* with impinging jets without fins. The results can be used to compare them with the results of the *SAH* after adding fins to ensure that the study results are good and explain the effects of adding fins to the *SAH*.

Table 3.1. Results of the smooth *SAH* with impinging jets.

Re	T_{pm} $[K]$	T_{out} $[K]$
10000	325.255	311.056
15000	317.570	307.393
20000	313.474	305.561
25000	311.007	304.425

3.2.1. Comparing the Fin Shapes

Table 3.2, Table 3.3, and Table 3.4 show the results of the simulations for all fin shapes. It is found that the main plate temperature is inverse proportion to the thermal efficiency, when the T_{pm} temperature decreases the thermal efficiency increase because of the high effectiveness of the convection heat transfer that occurs by cooling. Main plate temperature (T_{pm}) and outlet temperature (T_{out}) are both related with the Nusselt number, so attention must be paid on the value of the Nusselt number because higher value of Nusselt number means higher convection heat transfer, so higher efficiency occurs.

3.2.1.1. Rectangular Fin Shape

Table 3.2. Results of the *SAH* with impinging jets and rectangular fins.

Re	**Fin Height [mm]**	**T_{pm} [K]**	**T_{out} [K]**
10000	1.25	319.440	308.492
10000	2.5	319.613	308.521
10000	3.75	319.543	308.484
10000	5	319.913	308.442
15000	1.25	313.543	305.655
15000	2.5	313.732	305.686
15000	3.75	313.513	305.657
15000	5	313.619	305.626
20000	1.25	310.438	304.233
20000	2.5	310.524	304.262
20000	3.75	310.410	304.231
20000	5	310.464	304.223
25000	1.25	308.579	303.399
25000	2.5	308.739	303.398
25000	3.75	308.528	303.386

25000	5	308.721	303.374

Figure 3.26 and Figure 3.27 show the variations of efficiency of the *SAH* and *Nu* number with the Reynolds number. It is obtained that adding rectangular fins increases the efficiency and Nusselt number. Also, it can be observed that the efficiency and Nusselt number take the highest values when the lower Reynolds numbers with the smaller fin height (1.25 *mm*). The difference between the efficiencies of the fin height of 1.25 *mm* and 3.75 *mm* is too small, they are near to each other (it is approximately 0.083 %). When increasing the velocity, the highest efficiency and Nusselt number values are obtained at the fin height of 3.75 *mm* condition. It can be concluded that the best thermal efficiency case depends on the velocity of the working fluid, if it is working with lower velocity values it should be used for the lower rectangular fin heights. However, increasing the flow velocity, the higher fin heights are more appropriate.

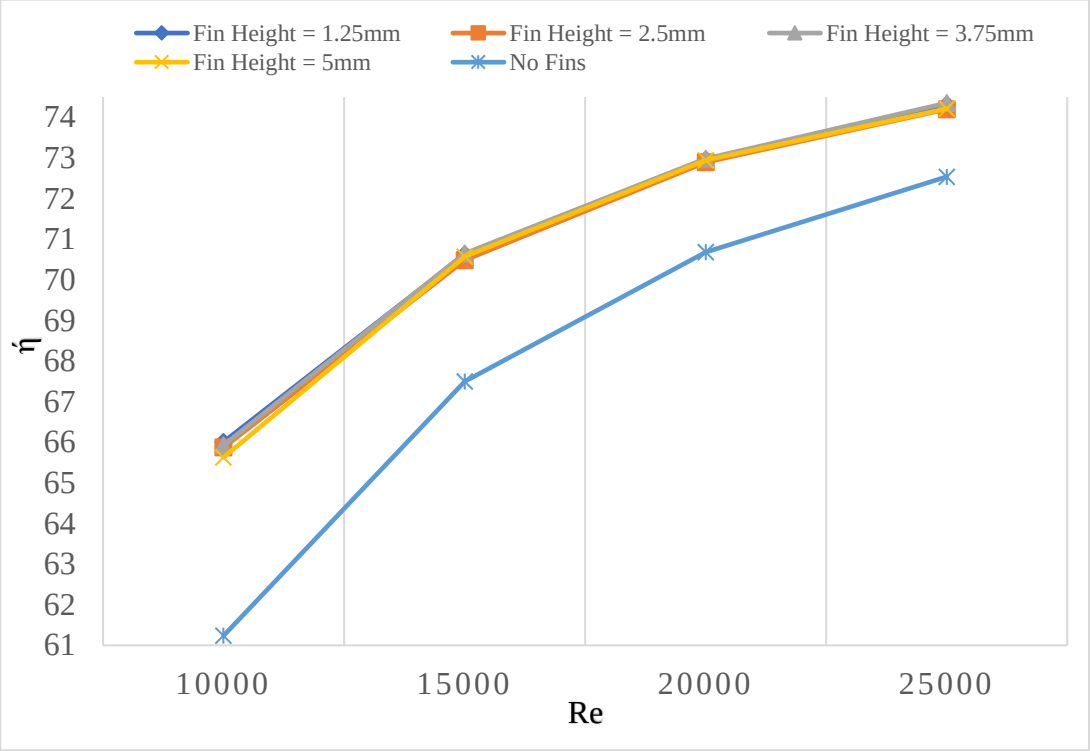

Figure 3.26. Variation of efficiency with Reynolds number for all fin's height values.

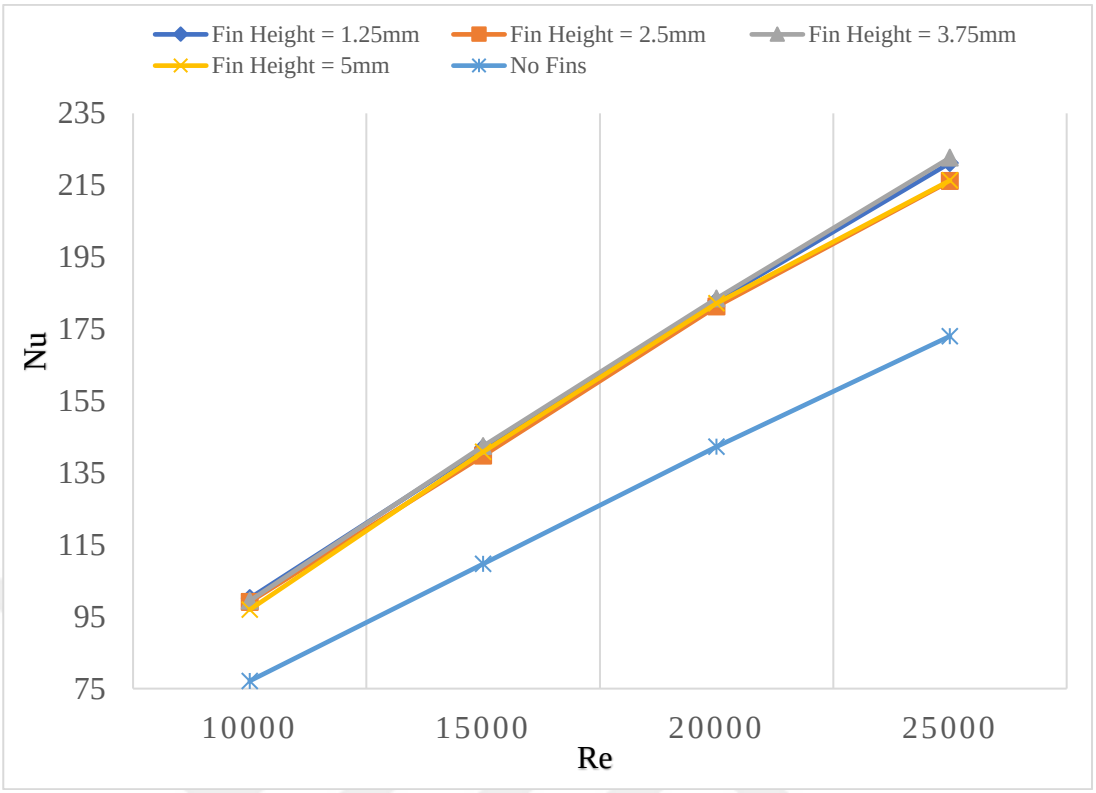

Figure 3.27. Variation of *Nu* with Reynolds number for all fin's height values.

Variation of pressure drop into *SAH* with Reynolds number is given in Figure 3.28. It is obtained that the pressure drop increases with adding fins. Also, pressure drop has small differences between the variety of the fin height. It is observed that the lower pressure drop is achieved in the case of 5 *mm* fin height. This condition gives the less pumping power than other fin heights.

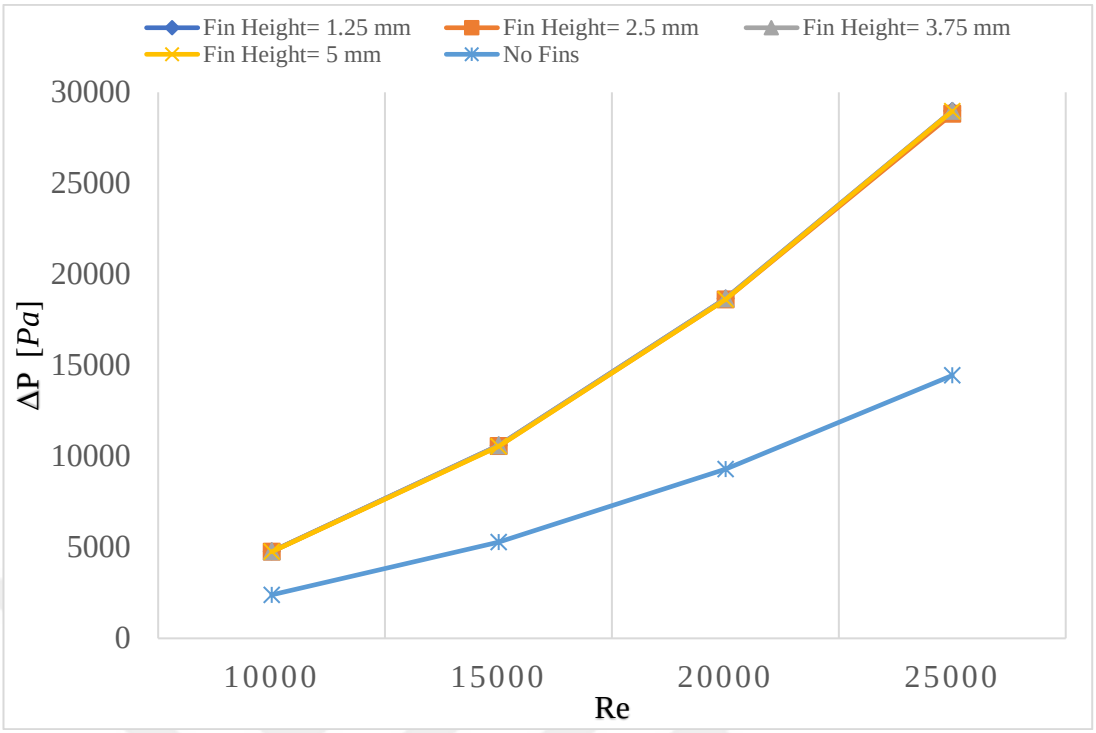

Figure 3.28. Variation of ΔP with Reynolds number for all fin's height values.

3.2.1.2. Circular Fin Shape

Table 3.3 presents the results of the *SAH* with impinging jets and circular fins.

Table 3.3. Results of the *SAH* with impinging jets and circular fins.

Re	***Fin Height [mm]***	T_{pm} ***[K]***	T_{out} ***[K]***
10000	1.25	320.142	308.830
10000	2.5	320.653	308.817
10000	3.75	320.835	308.830
10000	5	320.768	308.752
15000	1.25	314.139	305.851
15000	2.5	314.418	305.886
15000	3.75	314.472	305.887
15000	5	314.389	305.852
20000	1.25	310.945	304.423

20000	2.5	310.992	305.868
20000	3.75	311.162	304.392
20000	5	311.054	304.382
25000	1.25	309.001	303.523
25000	2.5	309.043	303.527
25000	3.75	309.137	303.510
25000	5	308.783	303.521

It is seen the variations of efficiency of the *SAH* and *Nu* number with Reynolds number in Figure 3.29 and Figure 3.30. It is obtained that adding circular fins increases the efficiency and Nusselt number. Also, it can be observed also that the efficiency and Nusselt number take the highest values when the lower Reynolds numbers with the smaller fin height (1.25 *mm*). When increasing the velocity, the highest efficiency and Nusselt number values are obtained at the fin height of 5 *mm* condition. It can be concluded that the best thermal efficiency case depends on the velocity of the working fluid. If the fluid is working with lower velocity values the lower circular fin heights should be used. Higher fin heights are preferable when the flow velocity is increased.

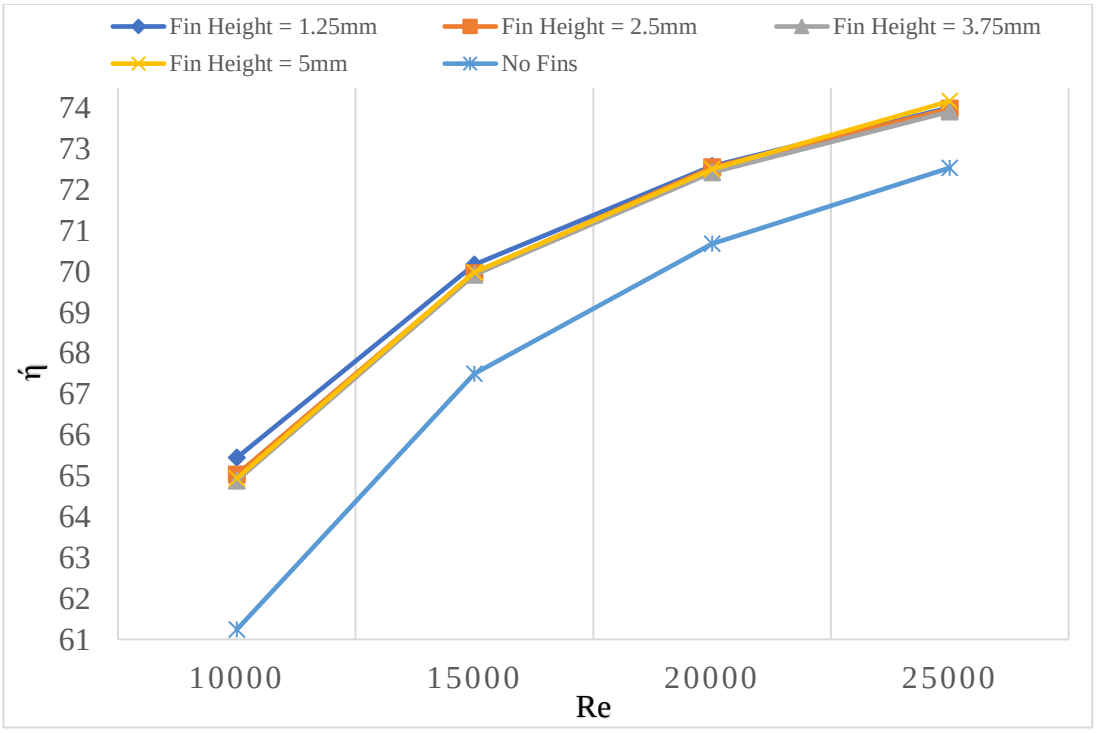

Figure 3.29. Variation of efficiency with Reynolds number for all fin's height values.

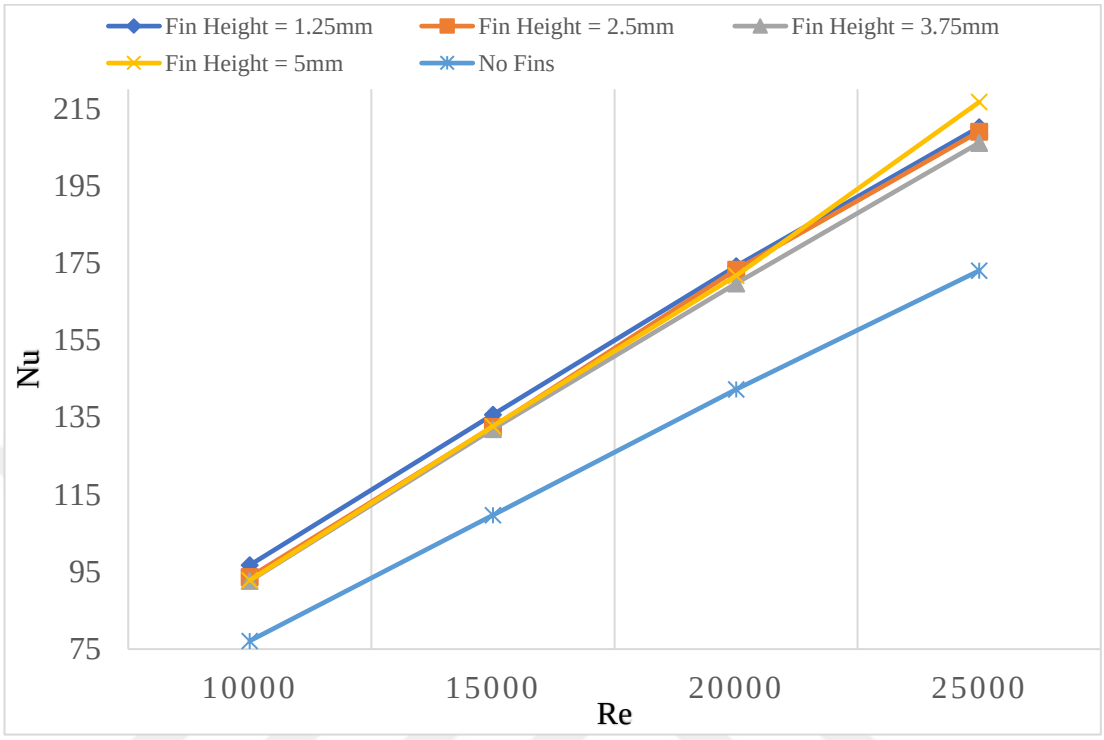

Figure 3.30. Variation of *Nu* with Reynolds number for all fin's height values.

Variation of pressure drop into *SAH* with Reynolds number is given in Figure 3.31. It is obtained that the pressure drop increases with adding fins. Also, pressure drop has small differences between the variety of the fin height. It is observed that the lower pressure drop is achieved in the case of 3.75 *mm* fin height. This condition gives the less pumping power than other fin heights.

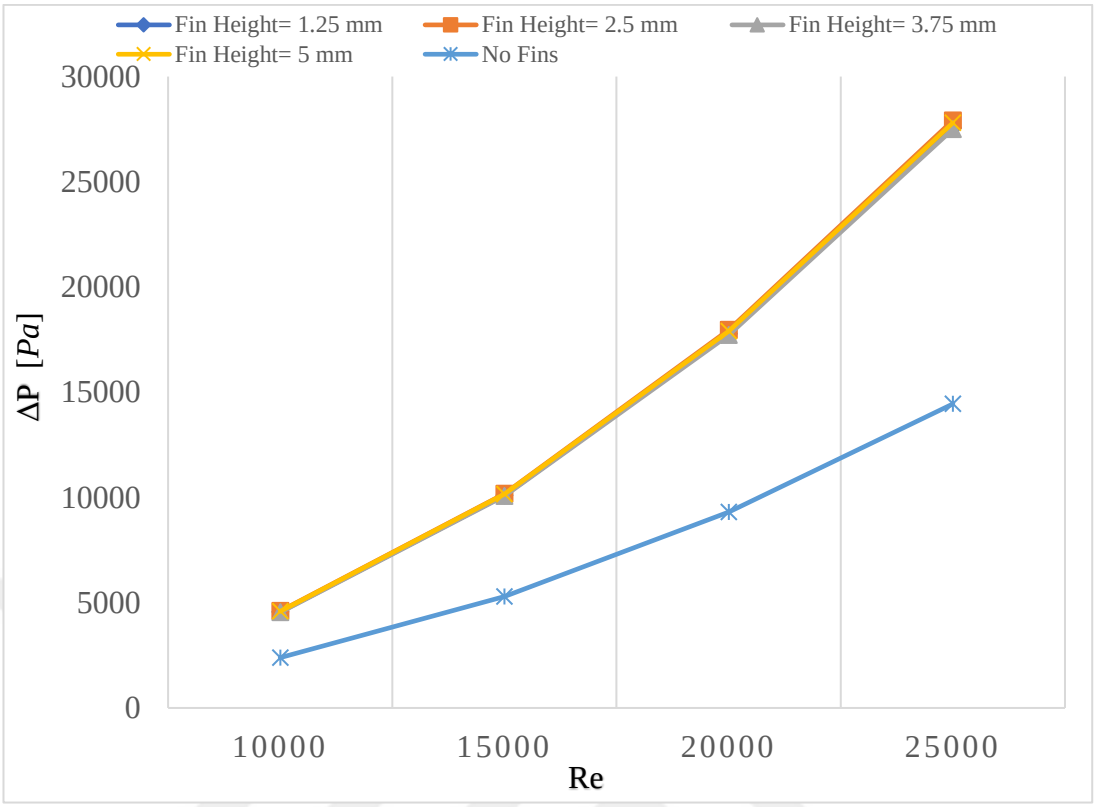

Figure 3.31. Variation of ΔP with Reynolds number for all fin's height values.

3.2.1.3. Triangular Fin Shape

Results of the *SAH* with impinging jets and triangular fins are given in Figure 3.4.

Table 3.4. Results of the *SAH* with impinging jets and triangular fins.

Re	***Fin Height [mm]***	T_{pm} ***[K]***	T_{out} ***[K]***
10000	1.25	319.856	308.809
10000	2.5	319.774	308.805
10000	3.75	319.789	308.799
10000	5	319.627	308.776
15000	1.25	314.123	305.808
15000	2.5	313.712	305.842
15000	3.75	313.780	305.875
15000	5	313.581	305.767

20000	1.25	310.783	304.379
20000	2.5	310.638	304.374
20000	3.75	310.575	304.414
20000	5	310.477	304.364
25000	1.25	308.860	303.509
25000	2.5	308.733	303.533
25000	3.75	308.633	303.507
25000	5	308.549	303.416

It is seen the variations of efficiency of the *SAH* and Nu number with Reynolds number in Figure 3.32 and Figure 3.33. It is obtained that adding triangular fins increases the efficiency and Nusselt number. Also, it can be observed that the efficiency and Nusselt number take the highest values at all values of Reynolds numbers with the bigger fin height (5 *mm*).

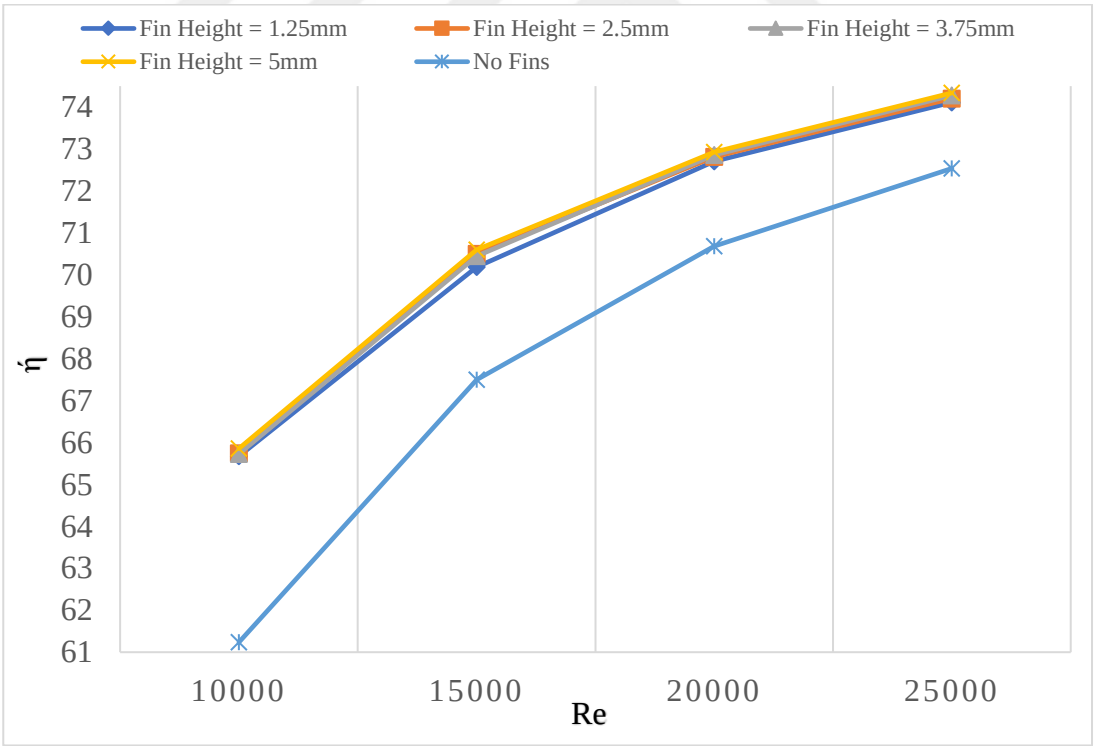

Figure 3.32. Variation of efficiency with Reynolds number for all fin's height values.

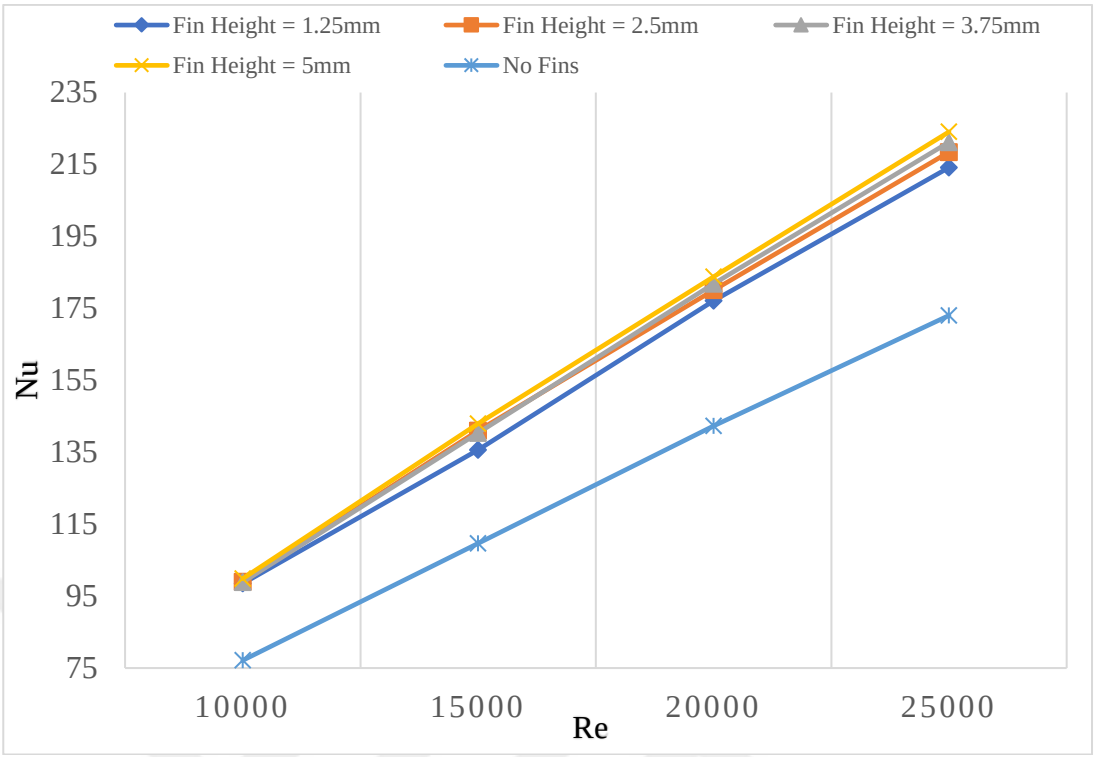

Figure 3.33. Variation of *Nu* with Reynolds number for all fin's height values.

Variation of pressure drop into *SAH* with Reynolds number is given in Figure 3.34. It is obtained that the pressure drop increases with adding fins. Also, pressure drop has small differences between the variety of the fin height. It is observed that the lower pressure drop is achieved in the case of 1.25 *mm* and 2.5 *mm* fin height, they have approximately same values. These conditions give the less pumping power than other fin heights.

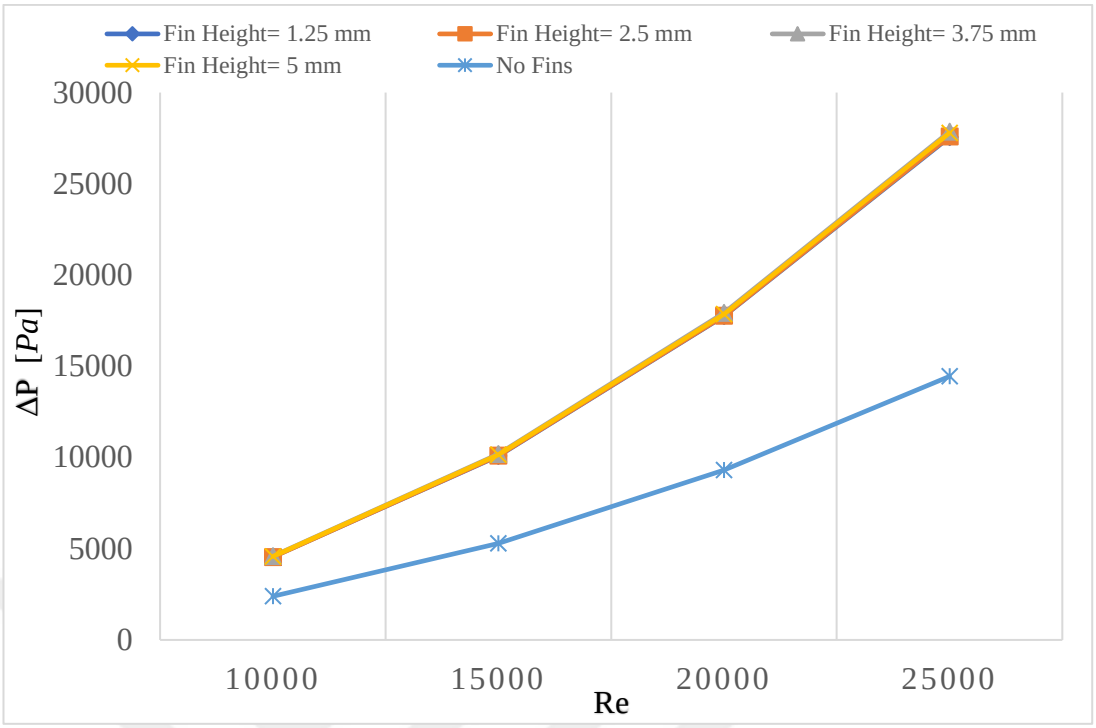

Figure 3.34. Variation of ΔP with Reynolds number for all fin's height values.

3.2.2. Comparison Of The Effects Of All Variable On The System Performance

The variation of efficiency with fin height for all fin shapes with *Re* is shown in Figure 3.35 and variation of Nusselt number with fin height for all fin shapes with *Re* is shown in Figure 3.36. When the *Re* is at 10000, it is found that the best choice to take the highest efficiency of (66.01%) and highest Nusselt number of (100.154) is for a rectangular fin shape at when the fin height equals (1.25 *mm*). When the *Re* is at 15000, it is found that the best choice to take the highest efficiency of (70.651%) and highest Nusselt number of (142.422) is rectangular fins at when the fin height is equal (3.75 *mm*). When the *Re* is 20000, it is found that the ideal choice to take the highest efficiency of (72.981%) and the highest Nusselt number of (183.461) is rectangular fins when the fin height is equal (3.75 *mm*). Rectangular fins with a fin height of (3.75 *mm*) are discovered to be the optimum option when Re is set to 25000 in order to achieve the highest efficiency and Nusselt numbers of (74.354%) and (222.645).

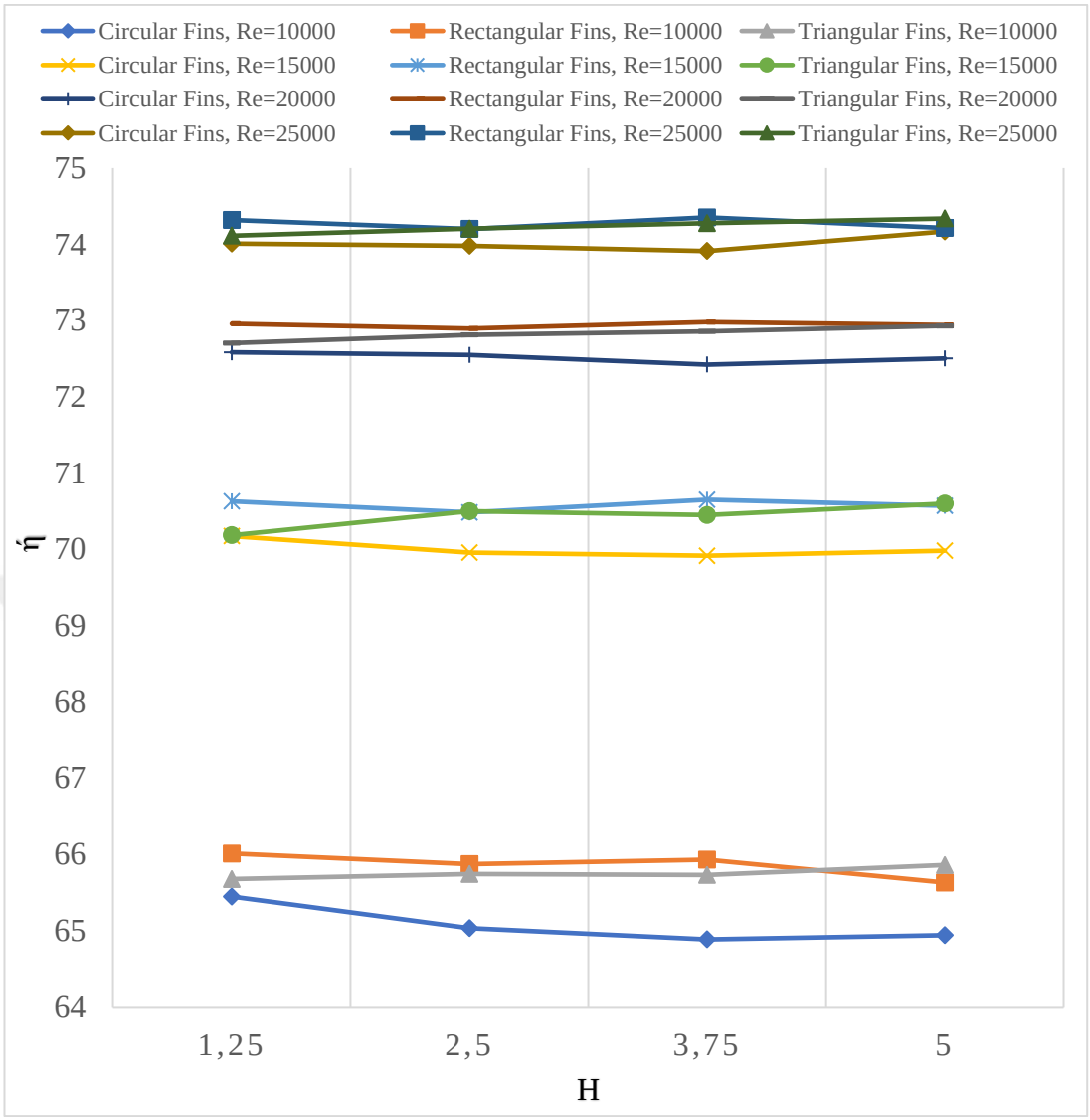

Figure 3.35. Variation of $\acute{\eta}$ with fin height for all fin shapes at all values of *Re*.

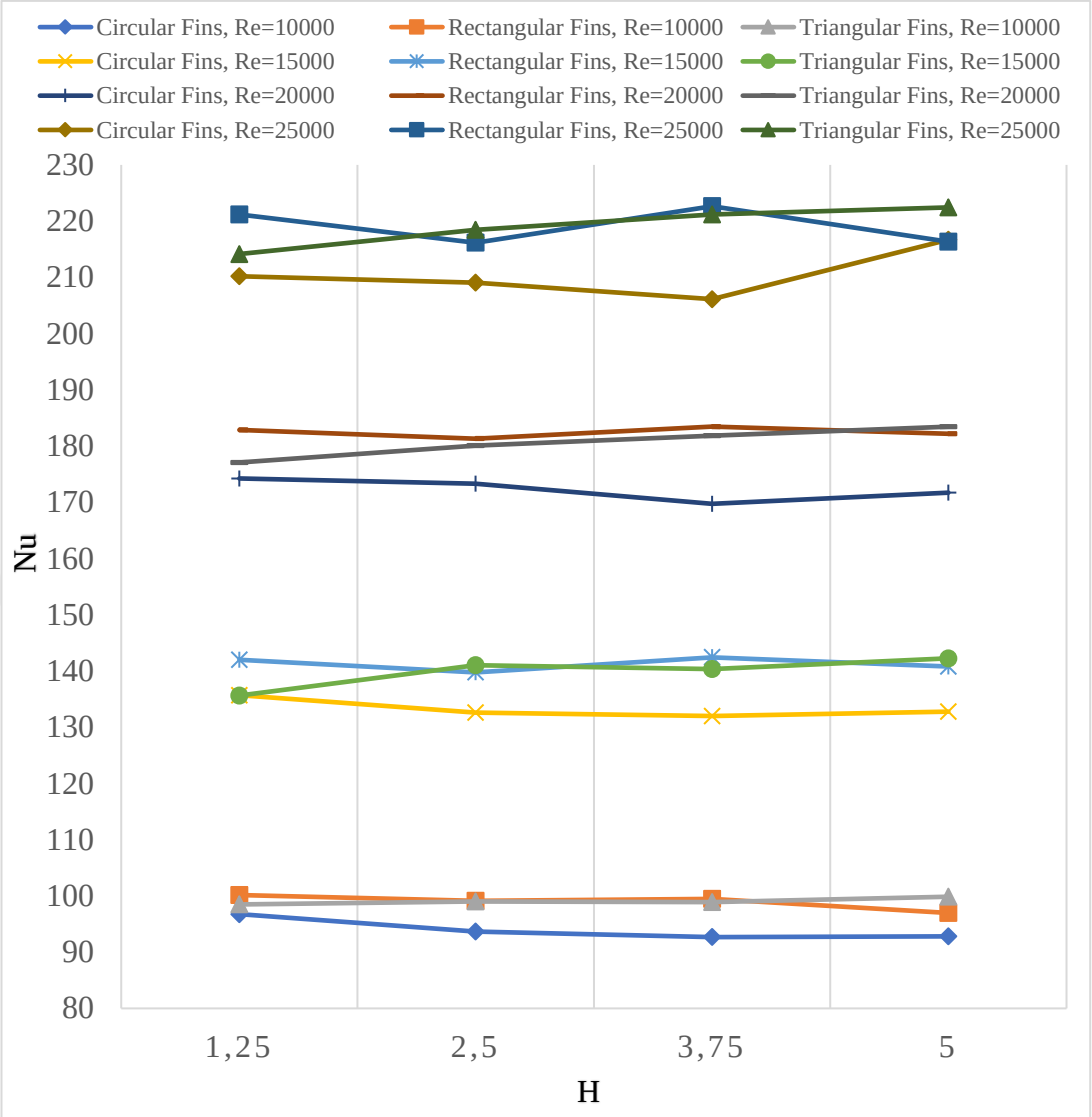

Figure 3.36. Variation of *Nu* with fin height for all fin shapes at all values of *Re*.

Variation of the pressure drop with fin height for all fin shapes with *Re* is shown in Figure 3.37. Despite the increase in efficiency with the increase of the Reynolds number, in return, the pressure drop increases, and thus the pneumatic cost of the system increases. The results indicate that the pressure drop changes very little with changing the fin height because of the small difference between the fin height values. In general, circular and triangular fins have approximately the same values of pressure drop, their pressure drop values are lower than the rectangular fins.

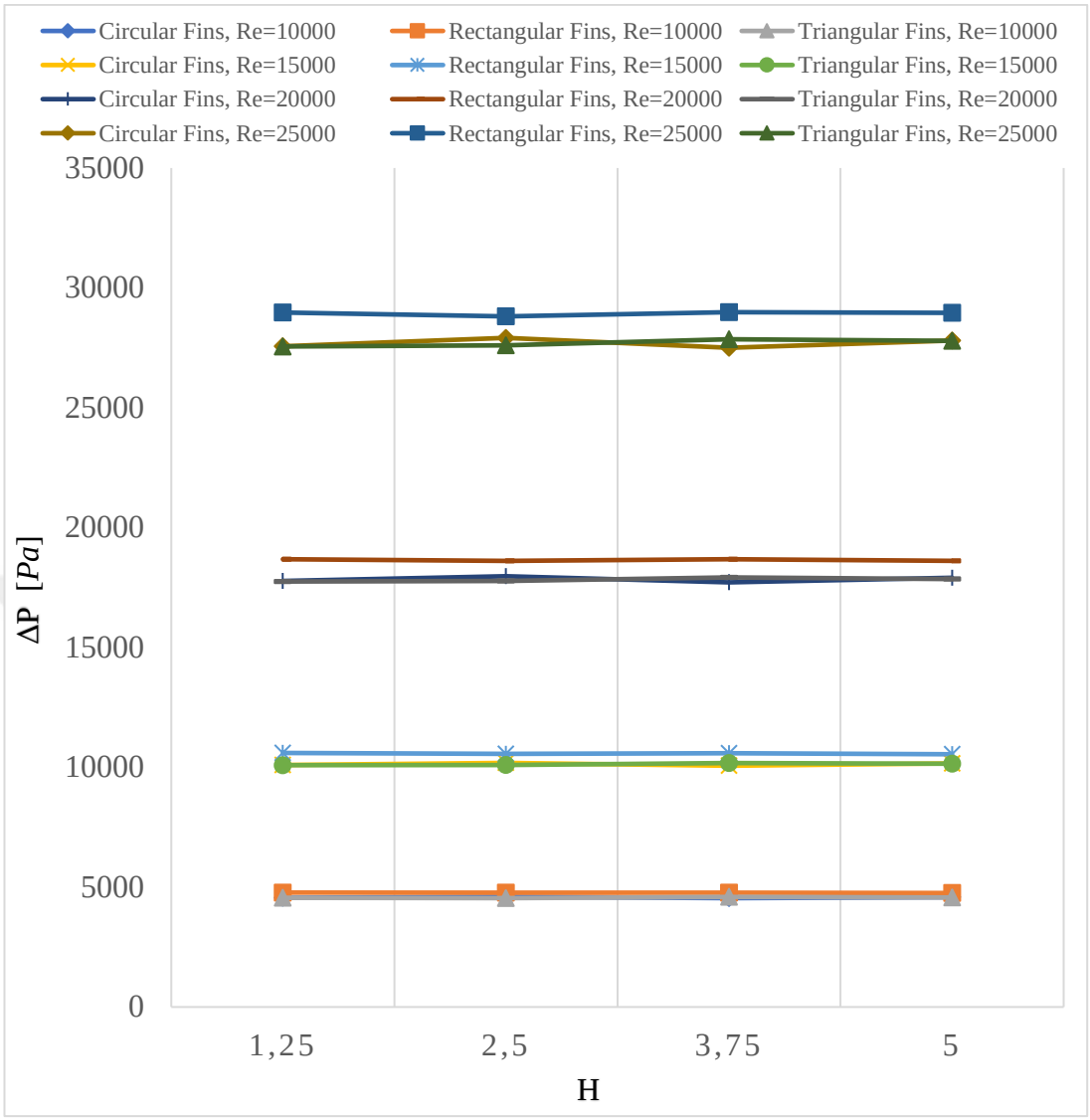

Figure 3.37. Variation of ΔP with fin height for all fin shapes at all values of *Re*.

PART 4

CONCLUSION

Due to the system simplicity, minimal material and upkeep costs, and long-running time, *SAH* will be one of the most useful technologies for several decades. In addition to small size that can allow it to be used for home or industry usage. The commercial type *SAH* has been studied in this thesis. Different types and heights of fins on the absorber plate surface have been used for increasing the efficiency of the *SAH*. *ANSYS* 2020 R2 has been used to design the *3D* model. After the calculations the following conclusions have been obtained:

1. The thermal efficiency and Nusselt number take the highest values when the lower Reynolds numbers with the smaller fin height (1.25 *mm*). Increasing the Reynolds number, the higher fin heights give better efficiencies.
2. Adjusting the fin height barely affects the pressure drop. In general, the pressure drop values of circular and triangular fins are smaller than those of rectangular fins, and they have roughly the same values.
3. The incorporation of fins enhances the thermal efficiency of the Surface Air Heat Exchanger (*SAH*) equipped with impingement jets. This enhancement stems from the augmentation of the heat transfer surface area, consequently leading to an escalation in the convective heat transfer cooling rate. In the case of a rectangular fin configuration, the most notable efficiency augmentation (7.23%) is observed at a Reynolds number of 10000. Similarly, the circular fin configuration demonstrates its peak efficiency increment (6.43%) at a Reynolds number of 10000. In the context of a triangular fin configuration, the utmost efficiency improvement (7.02%) is realized at a Reynolds number of 10000.
4. At a Reynolds number of 25000, it is observed that a rectangular fin configuration characterized by a fin height of 3.75 mm yields an elevated thermal efficiency of 74.354%.

5. Circular fin shapes give the minimum thermal efficiency values for all cases.

SUGGESTIONS FOR FUTURE WORK

In this part of the study, some topics that could improve the application if it is applied as a project are given

1. This study is done using the turbulent flow for the minimum Reynolds number of 10000. In future work, lower Reynolds numbers can be used.
2. In this study, the fin width is taken as constant at 10 *mm*. Thinner and thicker fin widthes can be tested to study the influences of the fin width on the convective heat transfer rate and thermal efficiency.
3. The diameter of the impinging jets have been set as constant at 3 *mm* in this study. Different jet diameters can be studied for obtaining the influence on the forced convection heat transfer rate.

REFERENCES

1. Pazarlioğlu, H. K., Ekiciler, R., and Arslan, K., "Numerical Analysis of Effect of Impinging Jet on Cooling of Solar Air Heater with Longitudinal Fins", ***Heat Transfer Research***, 52: (2021).
2. Matheswaran, M. M., Arjunan, T. V, and Somasundaram, D., "Analytical investigation of solar air heater with jet impingement using energy and exergy analysis", ***Solar Energy***, 161: 25–37 (2018).
3. Nwosu, N., "Employing Exergy-Optimized Pin Fins in the Design of an Absorber in a Solar Air Heater", ***Energy***, 45: 248–253 (2010).
4. Forsberg, C. H., "Introduction to heat transfer", ***Heat Transfer Principles And Applications***, 1–21 (2021).
5. Shahidian, A., Ghassemi, M., Mohammadi, J., and Hashemi, M., "Introduction", ***Bio-Engineering Approaches To Cancer Diagnosis And Treatment***, 1–22 (2020).
6. Hemmat Esfe, M., Esfandeh, S., and Kamyab, M. H., "History and introduction", ***Hybrid Nanofluids For Convection Heat Transfer***, 1–48 (2020).
7. Hall, M. R. and Allinson, D., "Heat and mass transport processes in building materials", ***Materials For Energy Efficiency And Thermal Comfort In Buildings***, 3–53 (2010).
8. Kosky, P., Balmer, R., Keat, W., and Wise, G., "Mechanical Engineering", ***Exploring Engineering***, 317–340 (2021).
9. Ghajar, A. and Cengel, Y., "Heat and Mass Transfer - Fundamentals and Applications, 6th Edition, ***McGraw-Hill Education***, New York, NY, 2020.", (2021).
10. Zohuri, B., "Forced Convection Heat Transfer", Thermal-Hydraulic Analysis of Nuclear Reactors, ***Springer International Publishing***, Cham, 323–345 (2017).
11. Camci, C. and Herr, F., "Forced Convection Heat Transfer Enhancement Using a Self-Oscillating Impinging Planar Jet", ***Journal Of Heat Transfer-Transactions Of The Asme - J HEAT TRANSFER***, 124: (2002).
12. Cengel, Y. A. and Ghajar, A. J., "Heat and Mass Transfer: Fundamentals and Applications", 5. Ed., ***McGraw-Hill Professional***, New York, NY, (2014).
13. Ferrari, J., Lior, N., and Slycke, J., "An evaluation of gas quenching of steel rings by multiple-jet impingement", ***Journal Of Materials Processing Technology***, 136 (1): 190–201 (2003).

14. Hollworth, B. R. and Berry, R. D., "Heat Transfer From Arrays of Impinging Jets with Large Jet-to-Jet Spacing", ***Journal Of Heat Transfer***, 100 (2): 352–357 (1978).

15. Singh, S., Chaurasiya, S. K., Negi, B. S., Chander, S., Nemś, M., and Negi, S., "Utilizing circular jet impingement to enhance thermal performance of solar air heater", ***Renewable Energy***, 154: 1327–1345 (2020).

16. Tepe, A. Ü., Yetişken, Y., Uysal, Ü., and Arslan, K., "Experimental and numerical investigation of jet impingement cooling using extended jet holes", ***International Journal Of Heat And Mass Transfer***, 158: 119945 (2020).

17. Pandya, B. and Karia, M., "A brief overview of application of extended surfaces (fins) for enhancement of heat transfer", ***Global Journal Of Engineering Science And Researches***, (2023).

18. Prasannakumaran, K. M., Sanjay Kumar, C., Karthikeyan, M., Premkumar, D., and Kirubakaran, V., "Chapter 31 - Nanopowdered biochar materials as a selective coating in solar flat plate collectors", Nanomaterials, ***Academic Press***, 663–676 (2021).

19. Moummi, N., Youcef-Ali, S., Moummi, A., and Desmons, J. Y., "Energy analysis of a solar air collector with rows of fins", ***Renewable Energy***, 29 (13): 2053–2064 (2004).

20. Kumar, R. and Chand, P., "Performance enhancement of solar air heater using herringbone corrugated fins", ***Energy***, 127: 271–279 (2017).

21. KARIM, M. and HAWLADER, M., "Performance investigation of flat plate, v-corrugated and finned air collectors", ***Energy***, 31 (4): 452–470 (2006).

22. Aboghrara, A. M., Baharudin, B. T. H. T., Alghoul, M. A., Adam, N. M., Hairuddin, A. A., and Hasan, H. A., "Performance analysis of solar air heater with jet impingement on corrugated absorber plate", ***Case Studies In Thermal Engineering***, 10: 111–120 (2017).

23. Safitra, A. G., Diana, L., Agil, D. M., Fareza, J. H., and Arini, N. R., "Thermal Analysis of Solar Air Heater with Ventilator Turbine and Fins", ***EMITTER International Journal Of Engineering Technology***, 8 (2): 510–523 (2020).

24. Nayak, R. K. and Singh, S. N., "Effect of geometrical aspects on the performance of jet plate solar air heater", ***Solar Energy***, 137: 434–440 (2016).

25. Bhushan, A., Kumar, R., and Perwez, A., "Experimental investigations of thermal performance for flat and dimpled plate solar air heater under turbulent flow conditions", ***Solar Energy***, 231: 664–683 (2022).

26. Yadav, S. and Saini, R. P., "Numerical investigation on the performance of a solar air heater using jet impingement with absorber plate", ***Solar Energy***, 208: 236–248 (2020).

27. Singh, S. and Negi, B. S., "Numerical thermal performance investigation of phase change material integrated wavy finned single pass solar air heater", ***Journal Of Energy Storage***, 32: 102002 (2020).

28. Omojaro, A. P. and Aldabbagh, L. B. Y., "Experimental performance of single and double pass solar air heater with fins and steel wire mesh as absorber", ***Applied Energy***, 87 (12): 3759–3765 (2010).

29. Kumar G. A., Singh, S. N., and Prasad, B. N., "Experimental investigation of thermo-hydraulic efficiency and performance characteristics of an impinging jet-finned type solar air heater", ***Sustainable Energy Technologies And Assessments***, 52: 102165 (2022).

30. Nayak, R. K., Prasad, R. S., Nayak, U. K., and Gupta, A. K., "Analytical study of thermal performance of a jet plate solar air heater with the longitudinal fins under the cross flow and non-cross flow conditions", ***Front. Heat Mass Transf.***, 19: (2022).

31. Goel, A. K. and Singh, S. N., "Thermal Performance of Solar Air Heater using Jet Impingement Technique with Longitudinal Fins", ***IIT(ISM) Dhanbad***, (2017).

32. Yunus A. Cengel and John M. Cimbala, "Fluid Mechanics: Fundamentals and Applications", 4. Ed., ***McGraw-Hill Education***, Columbus, OH, 1000 (2017).

33. Menter, F. R., "Two-equation eddy-viscosity turbulence models for engineering applications", ***AIAA Journal***, 32: 1598–1605 (1994).

34. Rehm, B., Consultant, D., Haghshenas, A., Paknejad, A. S., and Schubert, J., "Situational Problems in MPD", ***Managed Pressure Drilling***, 39–80 (2008).

35. Roy, U. and Roy, P. K., "Advances in heat intensification techniques in shell and tube heat exchanger", ***Advanced Analytic And Control Techniques For Thermal Systems With Heat Exchangers***, 197–207 (2020).

36. Boyce, M. P., "Combustors", ***Gas Turbine Engineering Handbook***, 427–490 (2012).

37. Hormozi Moghaddam, M. and Karami, M., "Heat transfer and pressure drop through mono and hybrid nanofluid-based photovoltaic-thermal systems", ***Energy Science & Engineering***, 10 (3): 918–931 (2022).

38. Chauhan, R. and Thakur, N. S., "Investigation of the thermohydraulic performance of impinging jet solar air heater", ***Energy***, 68: 255–261 (2014).

39. Duffie A. John and Beckman A. William, "Flat-Plate Collectors", Solar Engineering of Thermal Processes, ***John Wiley & Sons, Inc.***, Hoboken, NJ, USA, 236–321 (2013).

40. ANSYS, "ANSYS Fluent Tutorial Guide 2020 R2", 1. Ed., ***ANSYS, Inc.***, U.S.A., (2020).

RESUME

Anas KABLAN enrolled in the Mechanical Engineering Department at Karabük University in 2016 and graduated with a Bachelor's degree in 2020 with a 3.63 GPA. He is now studying for taking his Master’s degree at the same department. He is currently working as a technical support engineer in Media City in Istanbul.